Deep Resources Engineering 2 (2025) 100210

Contents lists available at ScienceDirect

Deep Resources Engineering

journal homepage: www.keaipublishing.com/en/journals/deepre/

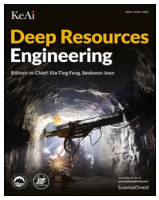

Full length article

Theories and applications of FRACOD – A fracture mechanics approach to modern rock engineering problems

Baotang Shen [a,b]

[a] CSIRO Mineral Resources, Brisbane, Queensland, Australia
[b] Shandong University of Science and Technology, Qingdao, China

ARTICLE INFO

Keywords:
Rock mass
Fracture
Propagation
Coupling
FRACOD
Thermal
Fluid flow
Geothermal

ABSTRACT

Rock failure is often governed by the initiation, propagation, and coalescence of fractures, particularly in hard rocks where fracturing, rather than plastic deformation, is the dominant failure mechanism. Therefore, predicting the explicit fracturing process is crucial when assessing rock mass stability for engineering applications. However, fracture mechanics are seldom employed in practical rock engineering design, primarily due to the limited understanding of complex fracturing processes in jointed rock masses and the absence of tools capable of accurately simulating these phenomena. Since the 1990s, a novel approach to modelling rock mass failure has emerged, utilizing a numerical code called FRACOD. This code, based on fracture mechanics principles, predicts the explicit fracturing processes in rocks. Over the past three decades, substantial progress has been made in advancing this method to the point where it can reliably predict rock mass stability at an engineering scale. FRACOD incorporates complex coupled processes, including thermal effects, rock mechanical response, and hydraulic flow, enabling it to address coupled problems commonly encountered in geothermal energy extraction, nuclear waste disposal, hydraulic fracturing, and underground LNG storage, etc. Numerous applications of FRACOD have been conducted over the last thirty years, including studies on borehole stability in deep geothermal reservoirs, pillar spalling under mechanical and thermal loading, and the prediction of tunnel and shaft stability, as well as the excavation disturbed zone (EDZ). This paper reviews the theoretical foundations of the fracture mechanics approach employed by FRACOD and highlights the most recent developments. It also presents several validation cases to demonstrate the accuracy of this approach. Additionally, a case study on geothermal energy development in the Cooper Basin, Australia, is included to illustrate the practical applications of this method.

1. Introduction

Rock fracture mechanics, evolving from the interaction of rock mechanics and fracture theory, has seen rapid progress in recent years, largely due to the increasing demand to understand rock mass failure mechanisms in both academic research and engineering practice. As geotechnical engineering moves into more complex domains such as deep mining, radioactive waste isolation, geothermal systems, and large underground structures, comprehending the coupled thermal, hydraulic, chemical, and mechanical (THCM) behaviours of rock masses becomes critical. In these processes, rock fractures serve as the dominant pathways for fluid transport and act as interfaces for thermal exchange, making fracture mechanics essential to understand them.

Over many decades, significant efforts have been made by researchers to develop various numerical techniques to predict fracture initiation and propagation behaviour. Early attempts were focusing on using finite element method for solving fracture propagation issues (e.g. [1]). However, the requirement of remeshing in standard FEM is a major disadvantage, and later the extended FEM is developed (XFEM) to specifically handle fracturing problems to avoid remeshing (e.g. [2]). Meanwhile, several other approaches have been developed and increasingly used for studying fracturing problems, namely the discrete element methods (DEM) (e.g. [3,4]), hybrid finite-discrete element method (FDEM) [5–7], smooth particle hydrodynamic (SPH) method [8–11], material point methods (MPM) [12]. These methods are mostly based meshed continuous approach (e.g. FEM, XFEM, MPM), or meshless particle based approach (e.g. DEM, SPH), each having advantages and disadvantages. The mesh-based approach treats fractures implicitly using special enrichment functions mathematically. While in most cases it simulates fracture propagation effectively, the implicit representation of an explicit

E-mail address: baotang.shen@outlook.com.

https://doi.org/10.1016/j.deepre.2025.100210
Received 25 July 2025; Received in revised form 29 August 2025; Accepted 30 August 2025
Available online 10 October 2025

fracture may miss some aspects of the true fracture behaviour. The particle based method, on the other hand, is excellent in investigating the micro-scale behaviours such as microcracking and Acoustic Emissions (AE), it often requires very significant computational resources to achieve a realistic representation of a real rock mass, hence it is difficult to be used on an engineering scale.

Currently, the need for design tools based on rock fracture mechanics has exceeded the availability of suitable numerical simulation methods. The majority of existing tools originate from civil and materials engineering, and are tailored for materials like metals, ceramics, glass, ice, and concrete whose fracturing behaviour significantly differs from that of rocks.

Since the early 1990s, researchers have initiated efforts to establish practical numerical models based on fracture mechanics principles for predicting rock failure behaviour. This modelling strategy stemmed from laboratory experiments and emerging insights into fracture propagation and linkage, especially the recognition of mode II (shear) fractures and their essential role in rock failure under compressive stress [13,14]. Building on this insight, a novel fracture criterion was developed [15,16], which allows for the prediction of both tensile and shear crack propagation, thus addressing the limitations of older criteria that considered only tensile failure. This criterion has shown strong predictive capability in simulating multi-fracture behaviour in rocks under laboratory conditions [17].

The initial development of this modelling technique was motivated by nuclear waste repository projects in Sweden and Finland, where fracture propagation due to thermal loading and glacial effects was identified as a critical risk [18,19]. During this phase, an early version of the FRACOD software was created, with capabilities for modelling fracture initiation, propagation, and acoustic emissions. Its functionality was later extended to incorporate time-dependent rock behaviour and subcritical crack growth [20]. Numerous case studies were carried out using FRACOD during its development, including Sweden's APSE pillar spalling tests, the DECOVALEX international collaboration, and investigations at the Mizunami Underground Research Laboratory in Japan.

This fracture mechanics-based modelling technique was later applied to additional rock engineering fields such as tunneling and geothermal development. For example, when assessing tunnel stability under high horizontal stress, FRACOD accurately reproduced the "log-spiral" fracture patterns observed in laboratory tests [21]. In a 4.4 km deep geothermal borehole in Australia, the method effectively simulated borehole breakout and enabled accurate back-analysis of the in-situ stress field [22].

Growing concerns over climate change have intensified global interest in alternative energy solutions and storage technologies. As a result, reliably predicting the interaction among fracturing, fluid transport, and thermal processes has become a critical scientific objective. FRACOD aims to tackle the intricate design challenges in emerging energy sectors, such as geothermal systems, underground LNG storage, and CO_2 geo-sequestration projects.

Since 2007, FRACOD development has been focused on coupling rock fracturing with thermal and fluid processes, enabled by international cooperation involving organisations from Australia, Europe, USA, China and South Korea. FRACOD has been enhanced to include Mechanical-Thermal-Hydraulic (MTH) coupling capabilities [23,24]. A wide range of case studies has been conducted using FRACOD, including applications in hydraulic fracturing, liquefied natural gas (LNG) underground storage, and spalling phenomena observed at nuclear waste disposal sites in Finland [25,26]. The method has also evolved into a fully three-dimensional FRACOD version to handle more realistic 3D fracture simulations [27].

This paper presents a comprehensive overview of the fundamental physical concepts and theoretical principles underpinning the FRACOD code. It also highlights representative engineering case studies where FRACOD has been successfully applied to solve real-world industrial challenges. For those who wish to read more details about FRACOD, please refer to the books "Modelling Rock Fracturing Processes" (1st & 2nd Editions) by [28,29].

2. Rock fracture propagation mechanisms and fracture criterion

Fracture behaviour of rocks fundamentally differs from that of homogeneous engineered materials like steel and glass. Underground rock fractures predominantly develop within a high-confining-pressure compressive regime, propagating through tensile, shear, and tearing modes. Shear fracture predominates as the main failure mechanism due to synergies between geostress fields and tectonic forces: high confinement suppresses tensile microcrack propagation, focusing damage energy into localized shear bands. Although the tensile strength of rock is substantially lower than its shear strength, compression-dominated geological settings significantly constrain tensile stress development, culminating in rock mass failure controlled by shear fracture initiation, slip coalescence, and sudden energy release.

Extensive laboratory experiments have investigated fracture propagation mechanisms in brittle rocks under compression. Petit and Barquins [30] conducted tests on sandstone and PMMA specimens with prefabricated flaws, revealing that uniaxial compression generates tensile wing cracks propagating along the major principal stress direction. Conversely, biaxial loading suppressed such cracks and triggered shear zones driven by Mode I microcracks, demonstrating that Mode II fault propagation represents a macroscopic phenomenon rather than a fundamental rupture mechanism. Shen et al. [14] performed uniaxial tests on gypsum specimens with parallel pre-existing fractures, showing that rock bridge failure mechanisms depend on geometric configuration: under low bridge inclination angles, secondary shear fractures (rough debris-covered surfaces) initiated at fracture tips caused coalescence; whereas high inclination angles led to coalescence via tensile wing cracks (smooth clean surfaces). Frictional interfaces increased shear failure loads by 35 %, confirming macroscopic shear fractures can occur independently while retaining microscopic tensile mechanisms. Rao [31] employed compression-shear, bending, and direct shear specimens to determine Mode II fracture toughness K_{IIc} (2–3 timesK_{Ic}, establishing a criterion where pure Mode II fracture occurs when $K_{II}^{\max} \geq K_{IIc}$ and $K_{I}^{\max} < K_{Ic}$, recommending compression-shear testing as the standardized method. Backers et al. [32] developed the Punch-Through Shear test (PTS-Test), measuring K_{IIc}on annularly notched cores under confining pressures ($\leq$70 MPa). Results demonstrated that beyond 30 MPa confining pressure, rock bridges undergo pure Mode II shear-dominated propagation with K_{IIc} stabilizing at rock-type-specific values. Collectively, these laboratory and field observations confirm that shear fractures can fully develop in rocks under compressive loading with confinement.

Fracture propagation in rock masses that involves both tensile and shear failure requires a unified criterion to predict both Mode I and Mode II fractures. Macroscopic fracture criteria generally fall into two principal categories: stress/strain-based approaches (e.g., maximum principal stress/strain criteria) and energy-driven mechanisms (exemplified by the strain energy release rate G criterion and strain energy density S criterion). Principal stress/strain criteria rely only on the maximum tensile stress or strain, and are therefore only applicable to Mode I fracture propagation. However, Mode II propagation requires consideration of both the principal stress/strain and the shear stress or strain. Energy-based criteria are more universal for predicting mixed-mode fractures, as the strain energy at the crack tip includes all components of stress and strain.

Empirical analyses of G and S-criterion applicability [17] confirm that neither criterion directly suits mixed-mode (I/II) fracture prediction. To address this limitation, Shen & Stephansson [16] improved the original G-criterion framework. The initial version simply stated that crack propagation occurs when the energy release rate reaches critical value G_c along its maximum direction – but failed to separate critical

energy thresholds for Mode I (G_{Ic}) and Mode II (G_{IIc}). Rock tests verify this mechanical difference [31], showing G_{IIc} typically exceeds G_{Ic} by two orders of magnitude in most engineered materials [33]. Because G_c must lie strictly between G_{Ic} and G_{IIc} for mixed-mode fractures, the traditional G-criterion shows major limitations in engineering practice.

Shen and Stephansson [16] proposed the F-criterion, a modified fracture criterion based on the G-criterion. This theory decouples the total strain energy release rate (G) at the crack tip into two components: the Mode I contribution (G_I) and Mode II contribution (G_{II}) (Fig. 1). The critical load and propagation direction are determined by the normalized sum $\frac{G_I}{G_{Ic}}+\frac{G_{II}}{G_{IIc}}$, where G_{Ic} and G_{IIc} denote the critical energy release rates for Mode I (tensile) and Mode II (shear) fracture propagation, respectively. Physically, G_I equals the energy dissipation in surrounding rock when a unit crack extension occurs under pure tensile deformation (no shear dislocation), while G_{IIc} corresponds to dissipation caused by pure shear deformation (no opening displacement). The principles of the F-criterion can be stated as follows:

(1) At an arbitrary propagation angle θ from the fracture tip, the fracture driving force $F(\theta)$ is calculated as:

$$F(\theta)=\frac{G_I(\theta)}{G_{IC}}+\frac{G_{II}(\theta)}{G_{IIC}} \tag{1}$$

(2) The fracture propagation direction θ_o corresponds to the angular position maximizing the fracture driving force $F(\theta)$, satisfying:

$$F(\theta)|_{\theta=\theta_0}=\max. \tag{2}$$

(3) The fracture tip will propagate when the maximum *F-value* reaches 1.0, i.e.

$$F(\theta)|_{\theta=\theta_0}=1.0 \tag{3}$$

The F-criterion fundamentally constitutes a generalized extension of the G-criterion, enabling unified characterization of Mode I/II fracture initiation. Analytical results demonstrate that peak F-values predominantly manifest along two principal strain orientations: the tensile-dominant direction (where G_I maximizes with $G_{II}=0$) and the shear-dominant direction (where G_{II} maximizes with $G_I=0$). This confirms single-mode propagation patterns - either pure Mode I or pure Mode II - consistently emerge at the elemental scale. Nevertheless, during actual propagation governed by dynamic adjustments in local stress fields, fracture modes may oscillate between Mode I and II, ultimately creating nonlinear propagation paths exhibiting hybrid failure signatures.

3. Theoretical background of FRACOD

The FRACOD code follows the Boundary Element Method (BEM) principle and uses the Displacement Discontinuity Method (DDM) as a core calculation method. This indirect boundary element technique combines fracture mechanics theories along with F-criterion to model fracture propagation process.

The DDM employed relies on the analytical solution of stresses and displacements generated when the constant displacement discontinuity occurs along finite line segment (e.g. crack) in a two-dimensional infinite elastic medium. Displacement discontinuity is defined as the displacement fields throughout the elastic medium that is continuous everywhere except over the line segment where they differ by a constant value. The analytical formula of this configuration, originally proposed by Crouch and Starfield [34], provides an explicit solution for the resulting stress field and displacement field. The stresses and displacements of a specific point can be found using Eq. (4).

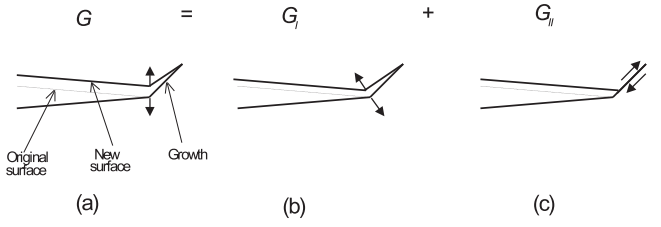

Fig. 1. Definition of G_I and G_{II} for fracture growth. (a) G, the growth has both open and shear displacement; (b) G_I, the growth has only open displacement; (c) G_{II}, the growth has only shear displacement.

$$\sigma_s=A_{ss}D_s+A_{sn}D_n$$

$$\sigma_n=A_{ns}D_s+A_{nn}D_n$$

$$u_s=B_{ss}D_s+B_{sn}D_n$$

$$u_n=B_{ns}D_s+B_{nn}D_n \tag{4}$$

Where D_s and $D_n$are the shear and normal components of displacement discontinuity. A_{ss}, etc., are the boundary influence coefficients of stress, while B_{ss}, etc., are the boundary influence coefficients of displacement respectively. The coefficients are the functions of elastic properties of solid body and the position of the point relative to the line segment, which represents the stresses or displacements of the point. The stress and displacement fields are caused by the discontinuity of the constant unit displacement.

For a crack of any shape, it is acceptable to represent it by N straight segments, joined end by end as shown in Fig. 2, provided that the number of line segment is sufficient. For each line segment, an elemental displacement discontinuity exists (D_s^j and D_n^j). Based on the principal of superposition and applying Eq. (4), the stresses and displacements at any point in the infinite body can be obtained. Applying the expressions to points on the line segments along the crack, the stresses and displacements have the form

$$\sigma_s^i=\sum_{j=1}^{N}A_{ss}^{ij}D_s^j+\sum_{j=1}^{N}A_{sn}^{ij}D_n^j$$

$$\sigma_n^i=\sum_{j=1}^{N}A_{ns}^{ij}D_s^j+\sum_{j=1}^{N}A_{nn}^{ij}D_n^j$$

$$u_s^i=\sum_{j=1}^{N}B_{ss}^{ij}D_s^j+\sum_{j=1}^{N}B_{sn}^{ij}D_n^j$$

$$u_n^i=\sum\nolimits_{j=1}^{N}B_{ns}^{ij}D_s^j+\sum\nolimits_{j=1}^{N}B_{nn}^{ij}D_n^j \quad \text{for i = 1 to N and j = 1 to N} \tag{5}$$

These equations together describe a *2 N*-element linear system of equations. These components D_n^j and D_s^j represent the basic displacement discontinuity elements. The solution is obtained by satisfying the *2 N* equations from Eq. (5) under prescribed traction and/or displacement conditions along the crack surface. When modelling rock mass discontinuities, the governing equations can incorporate multiple stress constraints including:

In the case of an open crack where stress transfer is impossible, the stress components in Eq. (5) are zero.

$$\sigma_s^i=0$$

$$\sigma_n^i=0 \tag{6}$$

In the case of a crack with surface elastic contact, the stress field can be expressed as a function of the crack stiffness (K_s,K_n) and the corresponding displacement discontinuity component, and has the following form

$$\sigma_s^i=K_sD_s^i$$

$$\sigma_n^i=K_nD_n^i \tag{7}$$

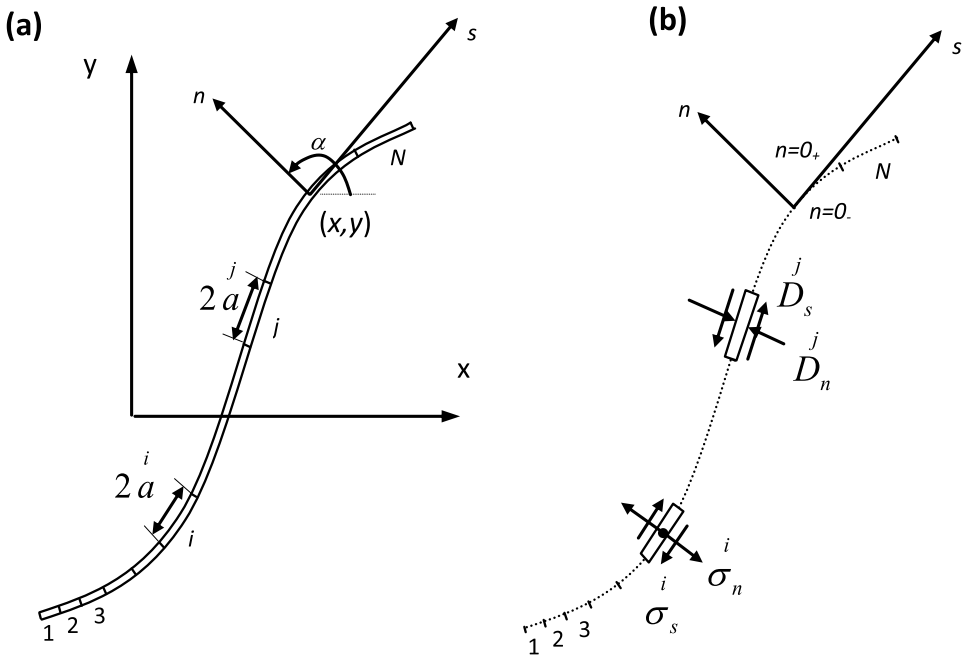

Fig. 2. Representation of a curved crack by *N* displacement discontinuity elements.

In the case of a crack with sliding surfaces, Coulomb's failure criterion is used.

$$\sigma_s^i = c + K_n D_n^i \tan\phi$$

$$\sigma_n^i = K_n D_n^i \tag{8}$$

where c is the cohesion strength and ϕ is the crack friction angle.

Finally, the unknown elemental displacement discontinuities (D_n^i and D_s^i) are determined by solving the governing equations in Eq. (5) through standard linear numerical methods, given properly defined boundary stress and displacement conditions.

The key step in using the F-criterion is to determine the strain energy release rate of mode I (G_I) and mode II (G_{II}) at a given fracture tip. As G_I and G_{II} are only the special cases of G, the problem is then how to use DDM to calculate the strain energy release rate G.

The G-value is defined as the change of strain energy when the crack propagates one unit of length in a linear elastic body. Therefore, the strain energy must be estimated first to obtain the *G-value*.

The strain energy, W, in a linear elasticity is

$$W = \iint_V \frac{1}{2}\sigma_{ij}\varepsilon_{ij} dV \tag{9}$$

where σ_{ij} and ε_{ij} represent the stress and strain tensors respectively, while V is the body's volume. Along its boundary, the strain energy can also be calculated from the stresses and displacements

$$W = \frac{1}{2}\int_s (\sigma_s u_s + \sigma_n u_n) ds \tag{10}$$

where σ_s, σ_n are the stresses in shear and normal direction along the boundary of the elastomer, while u_s, u_n are the displacements in shear and normal direction along the boundary of the elastomer. Applying Eq. (10) to a single straight crack in an infinite body with far-field stresses in the shear and normal direction of the crack, $(\sigma_s)_0$ and $(\sigma_n)_0$, the strain energy, W, in the infinite elastic body is

$$W = \frac{1}{2}\int_0^a [(\sigma_s - (\sigma_s)_0)D_s + (\sigma_n - (\sigma_n)_0)D_n] da \tag{11}$$

where D_s, D_n are the shear and normal displacement discontinuity of the crack and a is the crack length. In the calculation of crack stresses and displacement discontinuities, the strain energy can be calculated by the stresses and displacement discontinuities and the length (a^i) of the ith crack element. Then the strain energy from the whole crack is the sum of the energies of all elements

$$W \approx \frac{1}{2}\sum_i \left(a^i(\sigma_s^i - (\sigma_s^i)_0)D_s^i + a^i(\sigma_n^i - (\sigma_n^i)_0)D_n^i\right) \tag{12}$$

It is noted that the far-field stresses are transformed along the elemental directions for each element.

The G-value in the direction θ at a crack tip can be estimated by

$$G(\theta) = \frac{\partial W}{\partial a} \approx \frac{[W(a+\Delta a) - W(a)]}{\Delta a} \tag{13}$$

where *W(a)* is the strain energy governed by the original crack, and *W (a+a)* is the strain energy governed by a new crack consisting of the original crack and a small extension of a at the crack tip in the direction of θ (Fig. 2). In Fig. 3, a 'fictitious' element is introduced to the tip of the original crack with the length a in the direction θ. Both *W(a)* and *W (a+a)* can be determined easily by directly using DDM and Eq. (12).

In summary, if the shear displacement of the "fictitious" element is numerically set to zero, i.e. only normal displacement is allowed, the

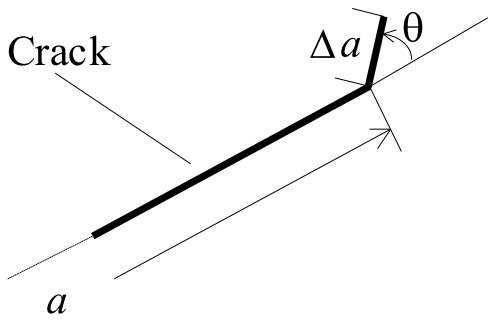

Fig. 3. A fictitious crack extension a at an angle θ relative to the initial crack orientation.

result obtained by Eq. (13) is $G_I(\theta)$. Similarly, when the normal displacement of the "fictitious" element is constrained to zero in the numerical model, the resulting value corresponds to $G_{II}(\theta)$. Once both $G_I(\theta)$ and $G_{II}(\theta)$ are determined, the *F-value* in Eq. (1) can be calculated by incorporating the known fracture toughness parameters G_{Ic} and G_{IIc} for the specific rock type under consideration. Then the maximum value of F and the corresponding direction can be sought. If the maximum value is equal to or greater than unity, then the crack will propagate in the maximum direction at the tip.

4. The coupling of rock fracturing and thermal-hydraulic processes

Over recent decades, coupled mechanical-thermal-hydraulic (M-T-H) processes in rock masses have received significant research attention, particularly within the context of underground nuclear waste disposal. Substantial advances in this domain are evidenced by foundational studies [35–37]. However, previous research has primarily modelled rock masses either as continuous media or as discontinuous structures with predefined fractures. The explicit simulation of rock fracturing, which plays a central role in the failure of hard rock, has not been sufficiently incorporated into the modelling of complex coupled processes. A fundamental challenge persists in predicting the coupled interactions between explicit rock fracturing, thermal transients, and fluid flow, specifically the interdependent Fracturing-Thermal-Hydraulic (F-T-H) processes governing rock mass behaviour. This challenge is particularly critical for industries involved in geothermal energy production, carbon dioxide storage in geological formations, underground liquefied natural gas storage, and the deep geological containment of nuclear waste.

In fragmented rock masses, the fracture of rocks, fluid flow and changes in rock temperature are closely related (Fig. 4). Rock fractures significantly increase hydraulic conductivity through the generation of new flow pathways and/or the dilation of pre-existing discontinuities, while fluid pressure may stimulate the growth of these fractures. Temperature changes induce thermal stress within the rock mass, potentially leading to fracture propagation. Moreover, there are secondary interactions among these three processes; for example, fluid flow can alter temperature, which subsequently affects the rock's stress state and may trigger further fracture propagation. Therefore, it is essential to incorporate coupling between these processes in numerical modelling for the aforementioned industrial applications.

To advance understanding of fracturing-fluid-thermal (F-T-H) coupling in geomechanical systems, recent FRACOD enhancements have prioritized modelling of rock fracturing processes interacting with thermal and hydraulic mechanisms. This section summarizes the theoretical background and numerical considerations of coupling the F-T-H functions in FRACOD.

4.1. Rock fracturing - thermal coupling

The direct coupling between rock rupture and the thermal process is a one-way coupling, the stress depends on the temperature field and follows the principle of thermo-elasticity. Leveraging the displacement discontinuity (DD) method - an indirect boundary element formulation - FRACOD consistently employs this numerical framework to simulate temperature field evolution and thermally-induced stresses driven by both volumetric heat sources and boundary heat fluxes. The method uses a virtual unknown heat source on the boundary, which makes it easier to consider the internal heat source problem [38]. A two-dimensional basic solution of temperature, stress, and displacement by the heat source of a unit strength at the origin of a thermoelastic coordinate system is given below.

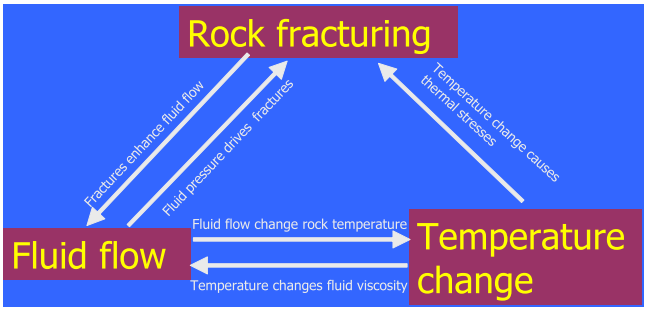

Fig. 4. Coupled interactions among rock fracturing, fluid flow, and thermal transients.

$$T = \frac{1}{4\pi k} Ei(\xi^2) \tag{14}$$

$$\sigma_{xx} = \frac{E\alpha}{8\pi k(1-\nu)} \left\{ \left(1 - \frac{2x^2}{r^2}\right) \frac{1 - e^{-\xi^2}}{\xi^2} - Ei(\xi^2) \right\} \tag{15}$$

$$\sigma_{xy} = \frac{E\alpha}{8\pi k(1-\nu)} \left\{ \left(-\frac{2xy}{r^2}\right) \frac{1 - e^{-\xi^2}}{\xi^2} \right\} \tag{16}$$

$$\sigma_{yy} = \frac{E\alpha}{8\pi k(1-\nu)} \left\{ \left(1 - \frac{2y^2}{r^2}\right) \frac{1 - e^{-\xi^2}}{\xi^2} - Ei(\xi^2) \right\} \tag{17}$$

$$u_x = \frac{\alpha(1+\nu)}{4\pi k(1-\nu)} r \left\{ \frac{x}{r} \frac{(1 - e^{-\xi^2})}{2\xi^2} + \frac{1}{2} Ei(\xi^2) \right\} \tag{18}$$

$$u_y = \frac{\alpha(1+\nu)}{4\pi k(1-\nu)} r \left\{ \frac{y}{r} \frac{(1 - e^{-\xi^2})}{2\xi^2} + \frac{1}{2} Ei(\xi^2) \right\} \tag{19}$$

where T is the temperature (°C), σ_{xx}, σ_{xy}, and σ_{yy} are the stresses (Pa), k is the thermal conductivity (W/m °C), ν is the Poisson's ratio, u_x and u_y are the displacements (m), α is the linear thermal expansion coefficient (1/°C), $r = \sqrt{x^2 + y^2}$, $\xi^2 = \frac{r^2}{4c_r t}$, $c_r = \frac{k}{\rho_r c_p}$, c_r is the thermal diffusivity (m^2/s), with ρ_r being the density (kg/m^3) and c_p being the specific heat capacity (J/kg °C), t is time (s), and $Ei(u) = \int_u^\infty \frac{e^{-z}}{z} dz$ in the above equations.

Eqs. (14)–(19) constitute the fundamental equations to be used in all the formulations of the numerical process for F-T coupling problems.

For the internal problem as shown in Fig. 5, the boundary of a finite field is discretized to n units. Before considering any mechanical boundary conditions, we assume that each element is in an infinite, isotropic, uniform medium to take advantage of the above basic solution. At time $t_0 = 0$, consider placing a constant line heat source with a unit heat intensity along element j. At any given time t, the temperature, stress, and displacement of the center point of another element (element i) are known from the basic solution given in Eqs. (14)–(19).

The heat source method assumes that one heat source is applied along each boundary source. The strength of these line sources are unknown and need to be addressed. For virtual sources and mechanical boundary conditions, the overall temperature change, stress and displacement of element i can be calculated by superimposition the effects of all single heat sources:

$$T^i = \sum_{j=1}^{n} T^{ij} H^j \tag{20}$$

$$\sigma_s^i = \sum_{j=1}^{n} (A_{ss}^{ij} D_s^j + A_{sn}^{ij} D_n^j + F_s^{ij} H^j) \tag{21}$$

$$\sigma_n^i = \sum_{j=1}^{n} (A_{ns}^{ij} D_s^j + A_{nn}^{ij} D_n^j + F_n^{ij} H^j) \tag{22}$$

$$u_s^i = \sum_{j=1}^{n} (B_{ss}^{ij} D_s^j + B_{sn}^{ij} D_n^j + G_s^{ij} H^j) \tag{23}$$

$$u_n^i = \sum_{j=1}^{n} (B_{ns}^{ij} D_s^j + B_{nn}^{ij} D_n^j + G_n^{ij} H^j) \tag{24}$$

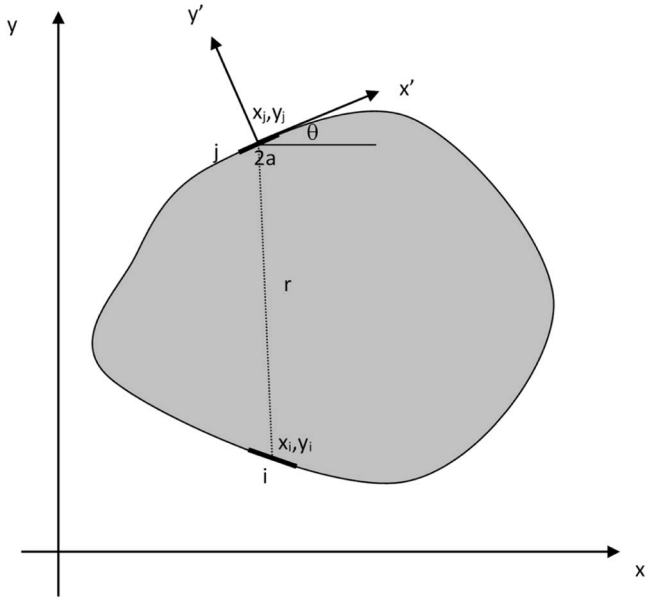

Fig. 5. Elements along a solid body boundary and local coordinate system of the boundary element.

where H^j is the strength of the line heat source at element j. T^{ij},$A_{ss}{}^{ij}$,$A_{sn}{}^{ij}$,$A_{ns}{}^{ij}$,$A_{nn}{}^{ij}$,$B_{ss}{}^{ij}$,$B_{sn}{}^{ij}$,$B_{ns}{}^{ij}$,$B_{nn}{}^{ij}$,F_s^{ij},F_n^{ij},G_s^{ij},G_n^{ij} are 'influence coefficients', representing the temperature, stress and displacement at the centre of the element i due to a unit strength line heat source and displacement discontinuities at element j. They are calculated based on the Eqs. (14)–(19) and those in Eq. (4). For example, due to the constant unit shear displacement discontinuity in the jth unit ($D_s^j = 1$)), the coefficient $A_{ns}{}^{ij}$ gives the normal stress (σ_n^i) at the midpoint of the ith unit.

Since the strength (H^j) of the provisional heat source depends on thermal conditions, it can be solved individually using only thermal boundary conditions. If the temperature along the boundary of the problem is known, then using Eq. (20) there are n equations and n unknowns. Then, by solving n linear equations, the virtual heat source strength can be obtained for each element. These values can be used in the Eqs. (21)–(24) to solve the sum of discontinuitiesD_s^j and D_n^j.

Alternatively, heat flux can be specified on a portion or the entirety of the boundary, instead of temperature. In this scenario, the flux condition substitutes the temperature-defined Eq. (20). Eq. (25) specifies the heat flux in the normal direction of element i resulting from a unit line source located at element

$$Q_{ij} = -k\frac{\partial T}{\partial n} = \frac{(x_i - x_j)\cos\theta_i + (y_i - y_j)\sin\theta_i}{8\pi k t^2} Ei(\xi^2) \tag{25}$$

The basic principle of the indirect boundary element method for thermoelastic analysis is to assume the existence of a virtual thermal source for each unit. The intensity (strength) of the source is unknown and is determined by boundary conditions. For example, if the temperature of all boundary elements is zero, the effect of the combination of boundary elements with all linear heat sources should be zero temperature. Once the strength of each virtual heat source is determined, temperature, heat flux, thermal induced stress and displacement at any given position in the rock can be calculated. By applying mechanical boundary conditions, displacement discontinuities on the unit can also be determined, and then the total stress and displacement at any given position can be determined.

4.2. Fracturing – hydraulic flow coupling

In fractured hard rock, fluids flow mainly through explicit cracks rather than through intact rock, which has a lower permeability. The movement of the cracks may be caused by the fluid pressure within the cracks, which may increase the aperture of the cracks or even induce crack propagation. Instead, this propagation alters the hydraulic conductivity and introduces new flow paths. The two-way interaction between fracture mechanics response and fluid dynamics is crucial for understanding the coupled fracture-hydraulic flow process.

Two primary methodologies have often been employed in modelling hydro-mechanical coupling within fractured rock media, namely the implicit and explicit methods. The implicit approach involves the concurrent resolution of the fluid flow equations with the mechanical equations that control the rock matrix and fractures. Most finite element programs that utilize Darcy's law for seepage simulation employ this approach.

A second approach, the explicit method, involves the simulation of fluid flow and mechanical response through an iterative process. This approach is well-illustrated in the commercial code UDEC [39], developed by Itasca. The explicit approach is less mathematically complex and more straightforward to handle complex and evolving model boundary conditions compared to the implicit approach. However, smaller time steps are typically required to ensure convergence, which in turn means longer computation times.

Explicit methods are employed in FRACOD, wherein mechanical calculations (including rock deformation and crack extension) are executed using a DDM with an iterative scheme to simulate the crack extension process. The calculation of fracture fluid flow is performed by means of an iterative method based on the cubic law [40], which is formulated primarily for fluid flow in rock fractures. It is noteworthy that the model incorporates a leakage mechanism from the fracture channel to the surrounding rock matrix.

In the mechanical numerical simulation employing the DD method, a fracture is subdivided into numerous DD elements. During the flow calculation, each DD element is designated as a hydraulic domain, with adjacent domains linked hydraulically (refer to Fig. 6). Fluid transfer between domains occurs in response to pressure disparities.

The numerical solution to the coupled F-H problem can be obtained using the iterative method presented in Fig. 7. Below, we provide a summary of this method.

Step1: The initial step in the process under investigation is the occurrence of fluid flow between fracture domains and the fluid leakage into the rock matrix. The Cubic law is employed to calculate the fluid flow between the fracture domains. The flow rate (Q) between two domains is calculated using Eq. (26):

$$Q = \frac{e^3}{12\mu}\frac{\Delta P}{l} \tag{26}$$

where e is fracture hydraulic aperture of the element domain; l signifies the element length, ΔP is defined as the two-element domain fluid pressure difference, and μ denotes the fluid viscosity.

The leakage from a fracture domain into the rock matrix is calculated using Eq. (27).

$$Q_{leak} = \frac{k_w}{\mu}\frac{P - P0}{d} \tag{27}$$

where k_w is rock permeability; The variable d represents the effective leakage distance, while P denotes the domain fluid pressure, and P_0 signifies the initial pore pressure. The effective leakage distance d is determined under the assumption that when measured d units away

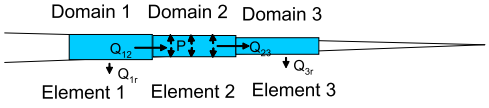

Fig. 6. Domain division for fluid flow simulation.

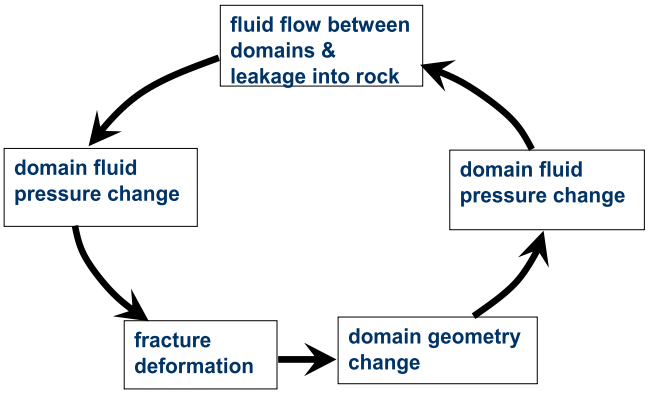

Fig. 7. Iterative process for a coupled F-H process.

from the fracture surface, the fluid pressure matches the initial pore pressure. Flow time and the configuration of the fracture system significantly impact the effective leakage distance. In the case of a long fracture characterized by constant internal fluid pressure, one-dimensional porous flow equations provide a suitable approximation, and it change over time. However, in cases involving irregular fracture networks, accurately determining the effective leakage distance becomes significantly more challenging. In such scenarios, this estimate should be regarded as a rough approximation only.

Step 2: This step involves the calculation of the change in pressure caused by the movement of a fluid within a specific domain volume. The new pressure caused by fluid movement over a short period of time can be calculated using Eq. (28):

$$P(t+\Delta t) = P_0 + E_w Q \frac{\Delta t}{V} - E_w Q_{leak} \frac{\Delta t}{V} \tag{28}$$

where E_w is the fluid bulk modulus; V is domain volume.

Step 3: A change in fluid pressure causes deformation of the fracture. Fracture deformation is computed using the DD method, with the updated fluid pressures in the fracture domains serving as input boundary stresses. Incorporating the fluid pressure within the fracture elements, the system of equations used to determine the element displacement discontinuities is presented in Eq. (29):

$$\begin{cases} (\overset{i}{(\sigma_s)}_0 = \sum_{j=1}^{N} \overset{ij}{A}_{ss} \overset{i}{D}_s + \sum_{j=1}^{N} \overset{ij}{A}_{sn} \overset{i}{D}_n - K_s \overset{i}{D}_s \\ (\overset{i}{(\sigma_n)}_0 + P(t+\Delta t) - P_0 = \sum_{j=1}^{N} \overset{ij}{A}_{ns} \overset{i}{D}_s + \sum_{j=1}^{N} \overset{ij}{A}_{nn} \overset{i}{D}_n - K_n \overset{i}{D}_n \end{cases} \tag{29}$$

During this step, the additional fracture deformation caused by any fracture propagation has also been considered and incorporated into the solutions.

Step 4: The deformation of the crack alters the volume of the region, thereby modifying the fluid pressure within that region. The new domain pressure is calculated using Eq. (30)

$$P'(t+\Delta t) = P(t+\Delta t) - E_w \frac{\Delta e \cdot l}{V} \tag{30}$$

Here Δe is the change of the fracture aperture at the element. The subsequent step involves the utilization of the new domain fluid pressure to calculate the flow rate between domains. It is imperative to reiterate the steps from 1 through 4 until the desired fluid time is attained and a stable solution is obtained.

During fluid flow calculation, an appropriate time step is required to ensure convergence of the iterative process to the final solution. This time step must satisfy the following condition.

$$\Delta t < \frac{12\mu \cdot l^2}{E_w \cdot e^2} \tag{31}$$

The convergent time step is influenced by both the fluid bulk modulus and the fracture aperture. Larger fracture apertures and higher fluid bulk moduli necessitate smaller time steps. For water at room temperature, with a fracture aperture of 50 micrometers and an element length of 0.1 m, the maximum allowable time step for fluid computation is approximately 2.4×10^{-5} seconds.

The time step derived from Eq. (31) applies to dynamic fluid simulations. However, in transient or steady-state flow problems, where the total simulation time may span days to months, such a small time step can make reaching a final solution computationally impractical. A common strategy to accelerate the calculation is to artificially reduce the fluid bulk modulus. Empirical observations suggest that using a lower bulk modulus not only enhances computational efficiency but also improves numerical stability in coupled simulations involving mechanical deformation.

4.3. Hydraulic flow – thermal coupling

Thermal disequilibrium between injected fluids and host rock induces intensive convective heat transfer within fracture networks, driving significant thermal energy exchange. This heat transfer mechanism not only affects the temperature state of the fluid itself, but also alters the thermal distribution characteristics of the surrounding rock mass. This is the basic principle of the geothermal energy operation where cold fluid is injected into a hot rock reservoir and hot fluid is extracted from the reservoir.

Coupling of fracturing-hydraulic flow in FRACOD only considers the flow behaviour of fracturing fluid inside the fracture, while ignoring the seepage effect dominated by pore structure in the rock matrix. In terms of heat transfer process, the heat transfer inside the rock mass is assumed to be completely controlled by the heat conduction mechanism, while in the fracture area, the process of fluid carrying heat is simplified to be dominated by convection. Considering that cracks usually have a small opening and the space occupied by fluids is relatively narrow, it is assumed that the temperature on the thickness of this layer is uniform and the same as the temperature on the rock wall.

Consider a simplified scenario illustrated in Fig. 8, where fluid flows from Fracture Domain i to Domain j. The rock temperatures at elements i and j are denoted as T_i and T_j, respectively. The fluid entering Domain j from Domain i initially maintains the temperature T_i. As the fluid traverses Domain j, heat transfer occurs between the fluid and the surrounding rock walls. Consequently, upon reaching the opposite end of Domain j, the fluid temperature equilibrates to T_j.

During this process, the fluid flowing through Fracture Domain j extracts thermal energy from the surrounding rock. This heat extraction effectively acts as a negative heat source for the rock, leading to a subsequent reduction in rock temperature. For a time duration of Δt, the fluid flow rate entering Domain j from Domain i is Q_{ij}, see Fig. 8. The net flow volume entering Domain j is calculated by Eq. (32)

$$\Delta V_j = Q_{ij} \Delta t \tag{32}$$

The temperature of this amount of fluid changes from T_i to T_j in Domain j and this will cause change of the thermal energy of fluid in Domain j. The change of total thermal energy in the fluid can be calculated by Eq. (33).

$$\begin{aligned} \Delta W_j &= c_w \rho_w (T_j - T_i) \Delta V_j \\ &= c_w \rho_w (T_j - T_i) Q_{ij} \Delta t \end{aligned} \tag{33}$$

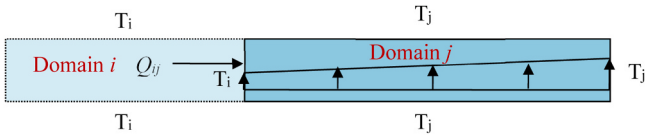

Fig. 8. Fluid flow inside Domain j.

where c_w is specific heat of the fluid and ρ_w is fluid density.

This is the thermal energy transferred from the rock mass to the fluid in Domain j. Note that Eq. (33) does not include the contribution from rock matrix flow (leakage) because there is no temperature difference between the fracture surface and the fluid from rock matrix.

The heat strength of this temporary heat source over the duration Δt will be calculated by Eq. (34).

$$H^j = \frac{\Delta W_j}{\Delta t} = c_w \rho_w (T_j - T_i) Q_{ij} \tag{34}$$

In the calculation process of time step Δt_{+1}, the current heat input should be determined based on the accumulated heat source intensity in all previous time steps. This processing method is consistent with the time stepping algorithm used in thermoelastic analysis, ensuring that the continuity and accumulation of thermal effects in the time domain are reasonably reflected.

The heat exchange between fluid and rock mass is a dynamically coupled and time-dependent interaction process. The fluid in the cracks will be heated during the flow process due to contact with rocks at higher temperatures, and at the same time, this process also leads to the gradual cooling of the rock mass due to the release of heat to the fluid. As the rock temperature decreases, the available thermal energy for transfer to the fluid diminishes, consequently reducing the magnitude of fluid temperature variations. In order to accurately capture this coupling behaviour, an iterative mechanism needs to be introduced in numerical solutions to gradually approximate and converge the nonlinear thermal interaction process between fluid and rock mass.

The numerical characteristics of the boundary element method inherently restrict the use of infinitesimal time increments when marching toward the final solution A practical way to achieve a final solution with a reasonable accuracy is to divide the problem time into a few rather large time steps. Due to the limited number of thermal steps permitted by the time-marching approach in the boundary element method, one will need to optimize the arrangement of the time steps. In general, the thermal strength curve should be more accurately modelled at the time closer to the problem time. The curve prior to this time duration may be simplified as they have less effect on the final solution. Consequently, computational efficiency can be optimized by employing an adaptive time-stepping strategy, where smaller time increments are implemented near the target simulation time while larger steps are maintained during earlier stages.

5. Validation and demonstration examples

For many years, FRACOD has been widely used in numerical simulations of field tests related to rock failure, and its effectiveness in predicting various rock mechanics behaviours has been verified. This method can simulate key engineering problems including borehole breakouts [41–43], brittle failure [44], pillar spalling [26,44], stability analysis of large vertical shafts and galleries [45], rock mass permeability evolution caused by fracturing [46], basic creep characteristics of rock samples [47], hydraulic fracturing [25], tunnel structure failure [43], and CO_2 geo-sequestration [48]. This section lists a few of these examples.

5.1. Modelling biaxial compressive test

The FRACOD method has been applied to numerical simulation studies of biaxial compression tests. This study constructed a numerical model that is similar in size to the actual laboratory samples, and applied biaxial compression loads to the samples in the simulation until they failed.

Now consider a biaxial compression experimental test using rock samples with dimensions of 120 mm × 60 mm. During the experiment, the top and bottom boundaries of the specimen were set to limit shear displacement to simulate a non-lubricated contact interface (i.e. high friction conditions). Vertical stress is applied to the upper and lower boundaries through a graded loading method, with each stress increment of 5 MPa, until the specimen undergoes overall instability and failure. A confinement stress of 10 MPa was used on the side boundaries. The intact rock was assumed to have a Young's modulus $E = 60$ GPa, Poisson's ratio $\nu = 0.25$, cohesion $c = 30$ MPa, internal friction angle $\phi = 30^\circ$ and tensile strength $\sigma_t = 13.4$ MPa. A Mohr-Coulomb strength criterion was used for fracture initiation. Random fracture initiation function in FRACOD was used and the initiation level was set to start at 50 % rock strength. The predicted process of fracture initiation and propagation during loading is plotted in Fig. 9. The locations and relative magnitude of Acoustic Emission (AE) events during the test are also given in Fig. 9. For the particular parameters used in this test, fracture initiation starts at a stress level of 80 MPa. Extensive failure occurred at an axial stress of 130 MPa.

Fig. 10 presents the stress-strain response curve obtained through numerical simulation in the loading experiment. When the stress-strain level reaches about 80 MPa, cracks start to initiate and the curve begins to deviate from the initial linear elastic stage, exhibiting nonlinear behaviour, which is consistent with the common rock material response in the laboratory. As the load continues to increase, cracks begin to expand and gradually interconnect at around 125 MPa, eventually forming a dominant shear failure surfaces under a peak axial stress of 130 MPa. After entering the post peak stage, the bearing capacity gradually decreases, and cracks continue to develop until the specimen loses much of its strength. After destruction, the material still retains a certain residual strength, about 60 MPa.

5.2. Cooling fractures in borehole wall

A borehole with a radius of $r = 0.1$ m, drilled into a hot geothermal reservoir, is analyzed using FRACOD to examine the potential for fracture initiation and propagation resulting from thermal stress in the borehole wall induced by cooling. The *in situ* rock temperature is $T_0 = 200\,^\circ$C, while the borehole wall is cooled by drilling fluid and kept at a temperature of $T_w = 80\,^\circ$C. The mechanical and thermal properties employed in this simulation are presented in Table 1.

Cooling durations of six distinct lengths were simulated: 10, 10^2, 10^3, 10^4, 10^5, and 10^6 seconds. Fracture initiation and propagation were analyzed during the final modelling stage. Fig. 11 illustrates the predicted thermal crack patterns adjacent to the borehole wall resulted from cooling. It was at the borehole wall that primary fracture initiation took place. These fractures propagated radially, merging with newly formed short fractures, ultimately developing into several extensive radial fractures. In other examples where the far-field stress state is anisotropic rather than hydrostatic as used in this example, the formation of one dominant cooling fracture is also observed in the direction of the major principal stress.

5.3. Rock mass cooling caused by fluid flow

During FRACOD's hydro-thermal coupling validation, a simple geothermal production case was simulated featuring a single open fracture within a homogeneous, isotropic, impermeable rock mass. The rock had an initial temperature T_{rock}. Fluid at a lower temperature T_{inj} was injected into the fracture at a constant flow rate Q. During fluid flow, the fluid will be heated by the hot rock, while the rock surrounding the fracture will be cooled by the fluid.

In this scenario, heat conduction takes place in the rock mass, while heat convection dominates within the fracture due to the flowing fluid. By neglecting heat conduction through the fluid and thermal conduction in the rock mass along the fracture direction, Bodvarsson [49] developed an analytical solution for temperature distribution along an infinitely long fracture, presented below.

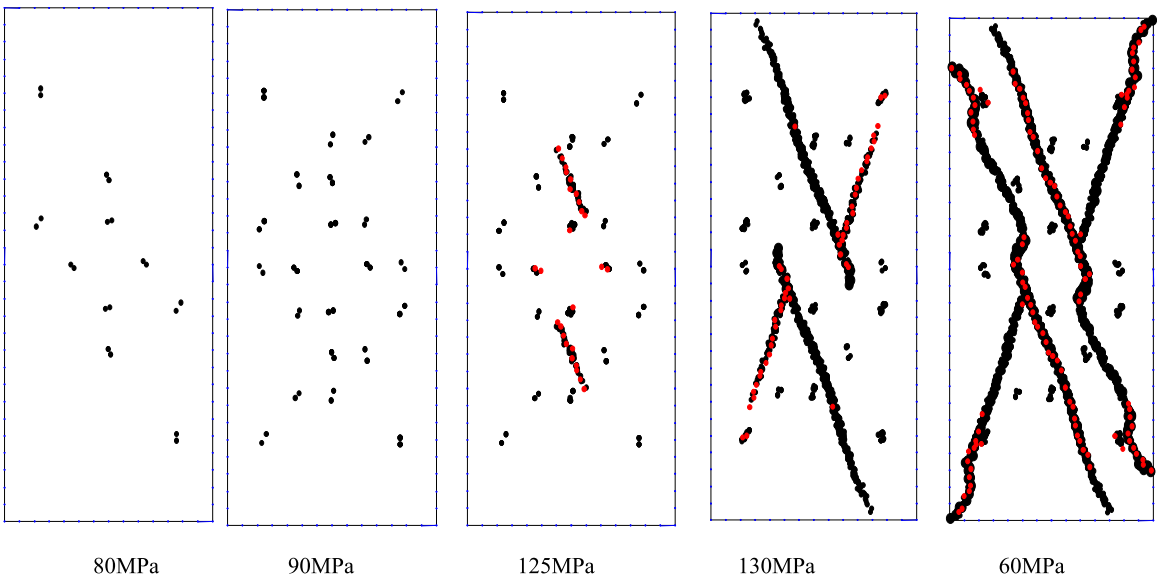

Fig. 9. Simulated fracture evolution of rock under biaxial compression.

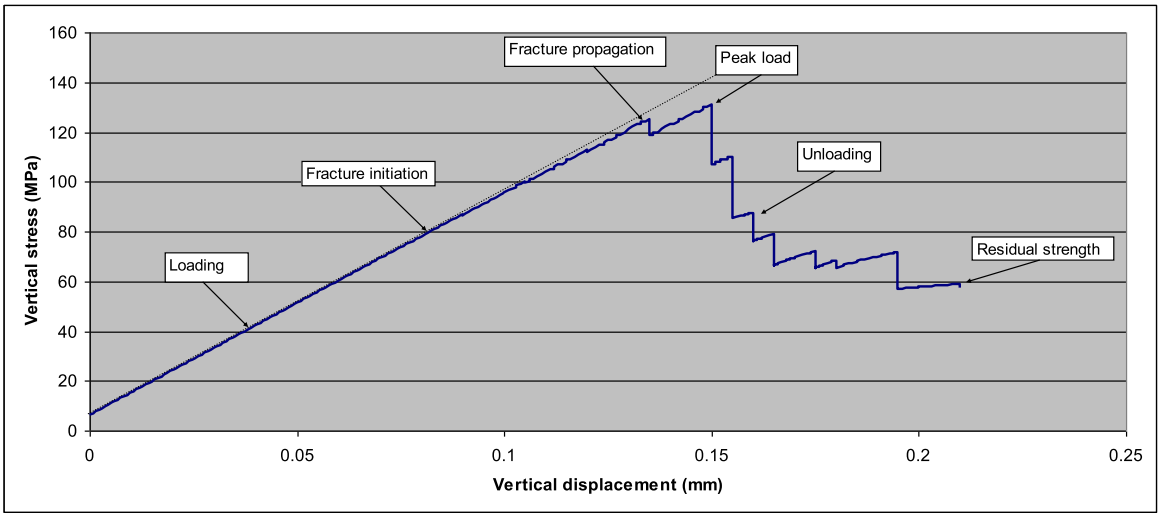

Fig. 10. The stress-strain relationship curve extracted based on the numerical biaxial compression test.

Table 1
Mechanical and thermal properties used in cooling fractures analysis in borehole wall.

Property	Value
Thermal conductivity (k)	10.07 W/m°C
Linear thermal expansion coefficient (α)	2.4×10^{-5} /°C
Specific heat (C_p)	790.0 J/(kg°C)
Poisson's ratio (ν)	0.25
Young's modulus (E)	37.5 GPa
Cohesion (c)	33 MPa
Tensile strength (σ_t)	12.5 MPa
Fracture Mode I toughness (K_{Ic})	1.5 MPa $m^{0.5}$
Internal friction angle (ϕ)	33°
In situ stresses ($\sigma_{xx} = \sigma_{yy}$)	10 MPa
Fracture Mode II toughness (K_{IIc})	3.0 MPa $m^{0.5}$

$$T(x) = T_{rock} - (T_{inj} - T_{rock}) \cdot \mathrm{erfc}\left[\left(\frac{k}{c_w Q \rho_w}\right)\frac{x}{\sqrt{bt}}\right] \quad (35)$$

Here

$T(x)$ – Temperature along the fracture at a distance x from injection point (°C);

T_{rock} – Initial rock temperature (°C);

T_{inj} – Temperature of injection fluid (°C);

k – Thermal conductivity of rock (W/m•°C);

c_w – Specific heat of fluid (J/kg•°C);

Q – Flow rate in fracture (m^3/s);

ρ_w – Density of fluid (kg/m^3);

b – Thermal diffusivity of rock (m^2/s).

For comparison between the analytical solution and the FRACOD model, a single fracture of 200 m length with a constant aperture of 100 μm is defined. Cold water is injected from one end of the fracture at a pressure of 50 MPa, while hot water is extracted from the other end at a constant pressure of 0 MPa.

Other rock and fluid properties used are listed below:

$T_{rock} = 200$ °C;

$T_{inj} = 80$ °C;

$k = 2.631$ W/m•°C;

$c_w = 4187$ J/kg•°C;

$Q = 4.24 \times 10^{-3}$ m^3/s;

$\rho_w = 1000$ kg/m^3;

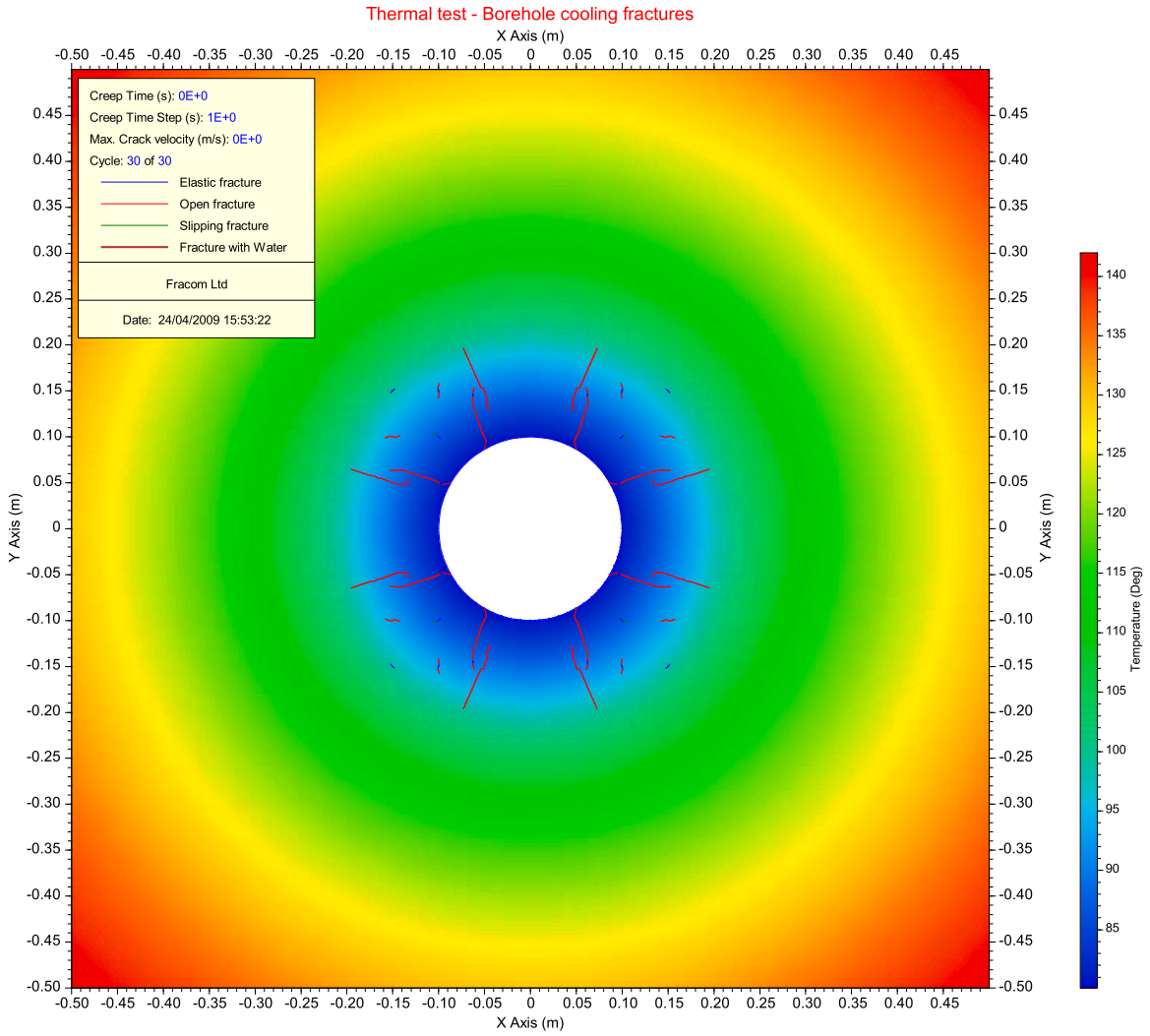

Fig. 11. Cooling fractures of a borehole. Predicted process of thermal cracks growth after 10^6 seconds of cooling.

$b = 1.48 \times 10^{-6}$ m^2/s.

Flow times of 0.5, 1, 2, 5, 10, 20, and 50 years were modelled. The modelled temperature variation along the fracture is shown in Fig. 12 for each time point, with comparison to Bodvarsson's [49] analytical solution.

The numerical results generally agree with the analytical solutions. However, because the FRACOD model considers a finite 200 m fracture whereas the analytical solution assumes an infinite fracture length, differences between the results are observed at longer flow times, e.g. 20 or e.g. 50 years.

Fig. 13 displays the simulated thermal distribution around the fracture across various time intervals. The cooling region progressively expands temporally. By Year 10, this zone extends to the extraction well at the fracture's terminus, initiating a decline in produced fluid temperature. After 50 years, the extracted fluid temperature is projected to stabilize at approximately 145 °C.

Cooling of the rock mass by flowing fluid generates localized tensile stresses that may drive propagation of pre-existing fractures. This scenario is examined by incorporating a pre-existing fracture near the main fracture (Fig. 14). After 10 years of production, thermally-induced stresses near the injection hole reach sufficient magnitudes to propagate the pre-existing fracture, causing it to coalesce with the main fracture. At the production hole side, however, thermal stresses remain significantly lower and insufficient for fracture propagation.

5.4. *FRACOD^{3D} - coupling of fracturing and fluid flow in fractures*

The three-dimensional version of FRACOD (FRACOD^{3D}) have been developed by Shi et al. [50] initially for mechanical function only and later extended to include thermal and hydraulic coupling [51]. FRACOD^{3D} uses the same numerical and fracture mechanics principles as the two-dimensional code, but the 3D nature of the code made it much more complex and challenging in terms of numerical formulations and computational process. Hence, to date, FRACOD^{3D} is only capable of simulating simple problems with very limited number of fractures. This section provides an example case of using FRACOD^{3D} to study a coupled problem where parallel fractures interact during fluid injection into the fractures.

A vertical borehole is drilled from ground surface (traction free surface) to a depth of 10 m and the borehole has a radius of 0.1 m. A horizontal circular fracture with radius of 4 m is used to represent the free surface. Two horizontal circular fractures are intersecting the borehole at locations of 5 m and 7 m below the free surface, respectively. Both fractures have a radius of 3 m and the initial aperture of 100 μm. The fluid pressure in the borehole is set as 10 MPa. Gravity and fluid leakage on the fracture surfaces are neglected. The fluid injection is from the borehole only. The material parameters used for rock are Young's modulus E = 5 GPa, Poisson's ratio $\nu = 0.2$, mode I fracture toughness $K_{Ic} = 10$ MPa m$^{1/2}$ and mode II and III fracture toughness K_{IIc}

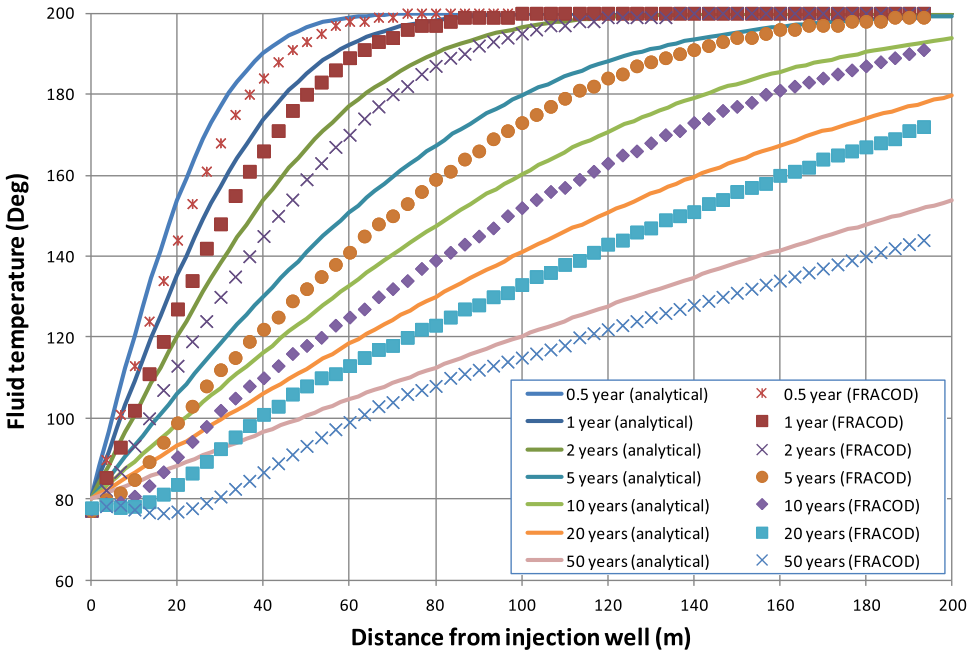

Fig. 12. Temperature distribution along a single fracture due to cool water injection in a geothermal reservior. Comparison of FRACOD results with analtical solutions.

$= K_{IIIc} = 1.0 \times 10^7$ MPa $m^{1/2}$ (this value effectively eliminates the possibility of mode II and III fracture propagation). The dynamic viscosity of the fluid is taken as $\mu = 8.9 \times 10^{-4}$ Pa s. Fig. 15 shows the simulation results of the coupling of fluid pressure and propagation of the fractures after three steps of propagation. Fig. 15a shows the configuration of the fractures and displacement field, and Fig. 15b shows the contour of aperture of the fractures. The pressure in the upper fracture pushes the free surface up. The interaction of the two fractures yield the dish-shaped fracture propagation paths and form the so-called "stress shadow" phenomenon. The free surface has some effect on apertures of the fractures: the upper fracture has slightly wider aperture than the lower fracture. The pressures in the fractures are very close to each other and this yields very small displacement between the two fractures (Fig. 15a).

6. Application – geothermal development in Australia

This section presents a study on estimating the magnitude of *in situ* horizontal stresses based on borehole breakout data from a deep geothermal well in Australia. Understanding *in situ* stress conditions is critically important for the efficiency of geothermal energy extraction, as it directly influences the shape and orientation of the subsurface heat exchange reservoir.

Extensive borehole breakouts were observed in the granite section (depth: 3650 – 4421 m) of the Habanero #1 well in the Cooper Basin during drilling operations [52]. The orientations and dimensions of these breakouts were measured using borehole logging tools. Due to the extreme downhole conditions, i.e. high temperatures (~ 240 °C) and significant overpressure (35 MPa above hydrostatic levels), direct stress measurement methods, such as hydraulic fracturing, could not be conducted. Consequently, the breakout data were the only information available for evaluating the *in situ* horizontal stresses.

The analysis was carried out using the FRACOD which has previously been validated for simulating borehole breakouts realistically [53,54]. A quantitative relationship between breakout dimensions and the magnitudes of *in situ* stresses in granitic rock was first established through numerical simulations. Then, the *in situ* stresses were back-analysed using this relation and the measured breakout dimensions through borehole logging at various borehole depths.

6.1. Numerical modelling of borehole breakouts

In this study, the focus lies solely on estimating horizontal stress magnitudes, while vertical stress is presumed to be governed by gravitational loading, calculated from overburden depth and rock density. Mechanical parameters considered include intact rock strength, fracture interface behaviour, and fracture toughness. Due to the absence of directly measured data for the Habanero #1 granite, parameter values were primarily adapted from previous numerical studies on similar granitic rocks (e.g., [45]). The values of the mechanical properties used in this study are listed below.

Intact rock strength:
Young's modulus = 65 GPa
Poisson's Ratio = 0.25
Cohesion = 31 MPa
Friction angle = 35 °
Uniaxial Compression Strength (σ_c) = 120 MPa
Fracture toughness:
Mode I toughness = 1.35 MPa $m^{1/2}$
Mode II toughness = 3.07 MPa $m^{1/2}$
Joint/fracture properties:
Normal stiffness *Kn* = 50,000 GPa/m
Shear stiffness *Ks* = 12,550 GPa/m
Friction = 25.5 °
Cohesion = 0
Dilation angle = 2 °

Fracture-related parameters have been shown to exert minimal influence on simulation outcomes once they exceed certain thresholds (e.g., sufficiently high stiffness and relatively low friction angle). The adopted values are deemed appropriate based on modelling experience with granite from Japan's Tono Mine and diorite from Sweden's Äspö Hard Rock Laboratory.

Numerical prediction of borehole breakouts follows a sequential procedure: First, a computational model is established incorporating borehole geometry, rock properties, and *in situ* stress conditions. Subsequently, the FRACOD algorithm computes borehole wall stresses via solid mechanics principles. Based on derived stress fields and rock strength parameters, the software evaluates fracture initiation potential along the borehole periphery. Upon detecting failure, new fractures are

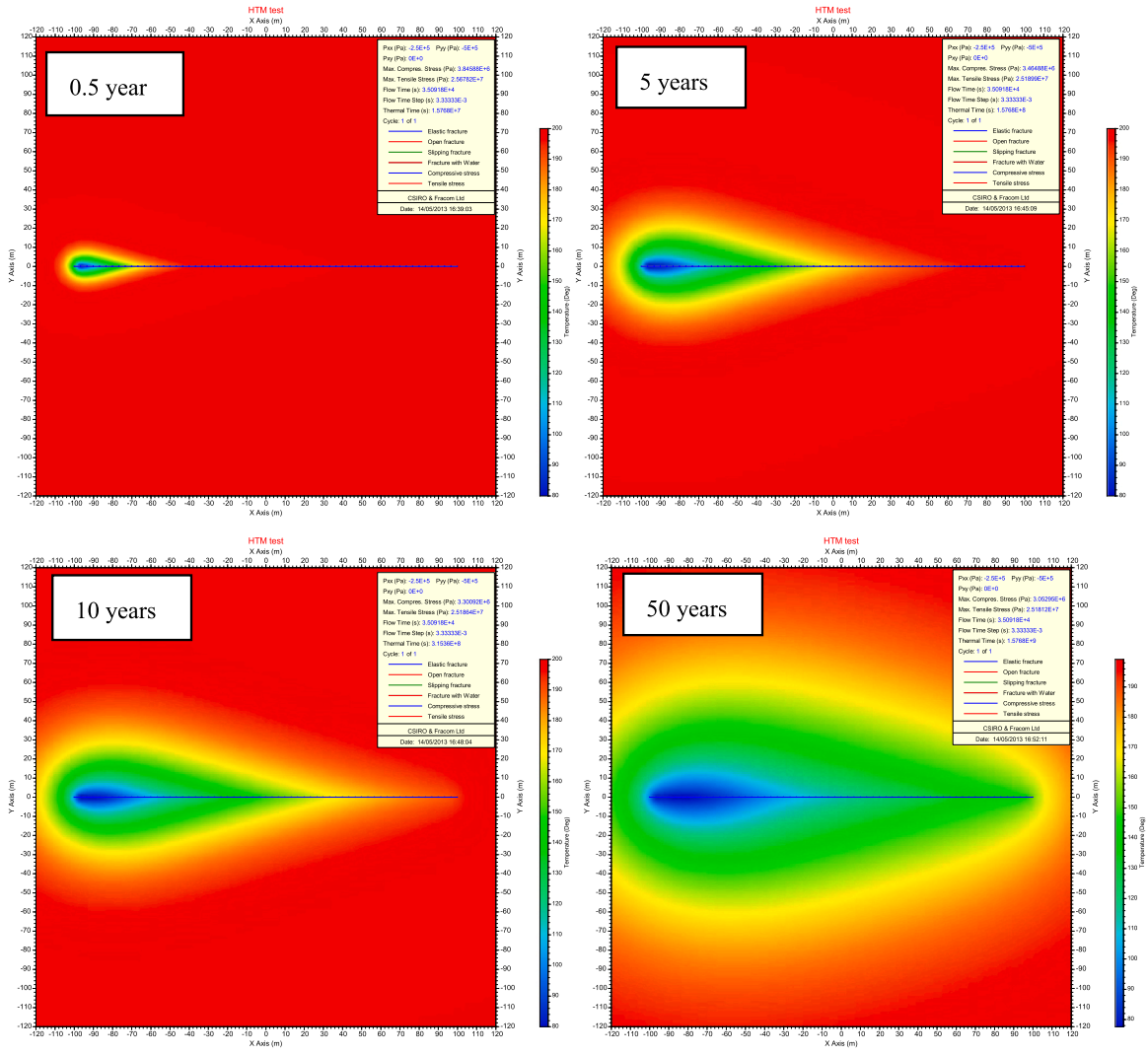

Fig. 13. Modelled temperature distribution in the vicinity of the fracture.

generated within the model, with FRACOD subsequently analyzing their propagation behaviour. Breakout formation occurs when wall fractures propagate and coalesce. Final breakout dimensions are recorded once fracture activity ceases.

Fifteen simulation cases with distinct horizontal principal stress combinations (σ_{Hmax} and σ_{hmin}) were executed (Table 2). Modeled σ_{Hmax} magnitudes spanned 50 – 80 MPa, while σ_{hmin} ranged from 10 to 60 MPa, yielding stress ratios ($\sigma_{Hmax}/\sigma_{hmin}$) of 1.2 – 8.0. Notably, all simulations employed effective stresses without pore pressure consideration.

Fig. 16 displays representative modelling outcomes, defining breakout angle as the azimuthal span of wall failure and breakout depth as the radial distance from the failure tip to the original borehole wall.

6.2. Back-analysis of horizontal stress magnitude

The analysis of the modelling results presented in Table 2 reveals the relationships between stress magnitude and breakout dimensions. The relations will be applied to predict the stress magnitudes based on observed breakout dimensions.

6.2.1. Correlations between stress/strength ratio and breakout angle

Elastic theory can be used to determine the tangential stress at a perfect borehole without fracturing. The azimuth angle where this stress exceeds the uniaxial compressive strength can be calculated using Eq. (36).

$$\frac{1-(\sigma_{Hmax}+\sigma_{hmin})/\sigma_c}{2(\sigma_{Hmax}-\sigma_{hmin})/\sigma_c}=\cos(\theta) \tag{36}$$

where

θ = breakout angle at the borehole wall (°)

σ_c = uniaxial compressive strength of rock (MPa)

Fig. 17 shows a comparison of the numerical and analytical results of relationship between stress/strength ratio and the breakout angle. A fairly good agreement is observed. This study employs a numerical method that incorporates the effect of progressive fracturing, while the analytical method does not involve this factor. The close agreement between numerical results and the analytical results indicates that the breakout angle is dominated by the initial stress distribution at the borehole wall, with the fracturing process having minimal affection.

6.2.2. Correlations between stress/strength ratio and breakout depth

The normalized depth of the breakout (breakout depth/borehole radius) is found to have a reasonable correlation with the ratio of the maximum tangential stress at the borehole to the rock's uniaxial compressive strength, as shown in Fig. 18. Nevertheless, discernible variations exist in the numerical results derived from the average

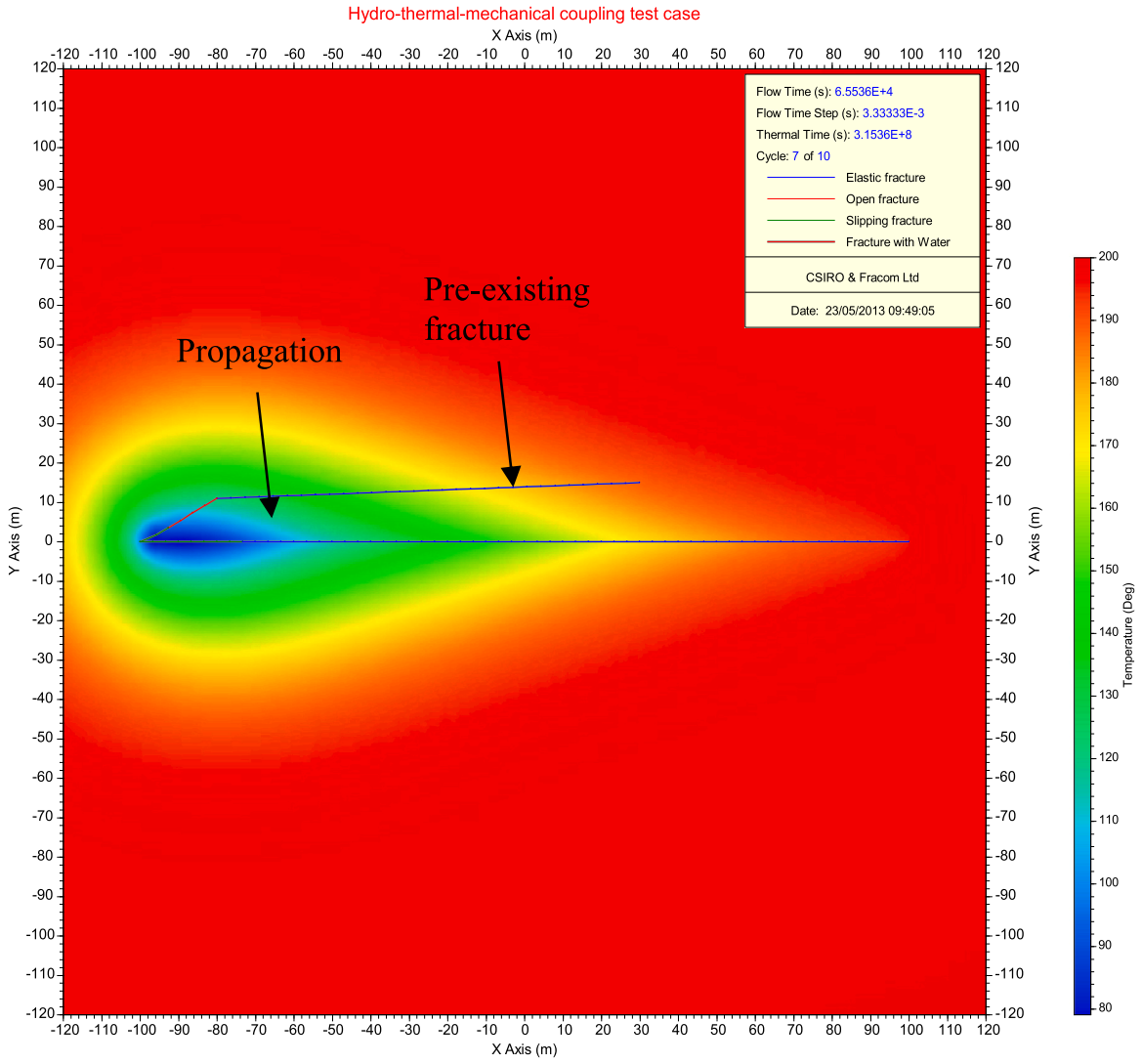

Fig. 14. Propagation of a pre-existing fracture due to cooling stress near the injection hole.

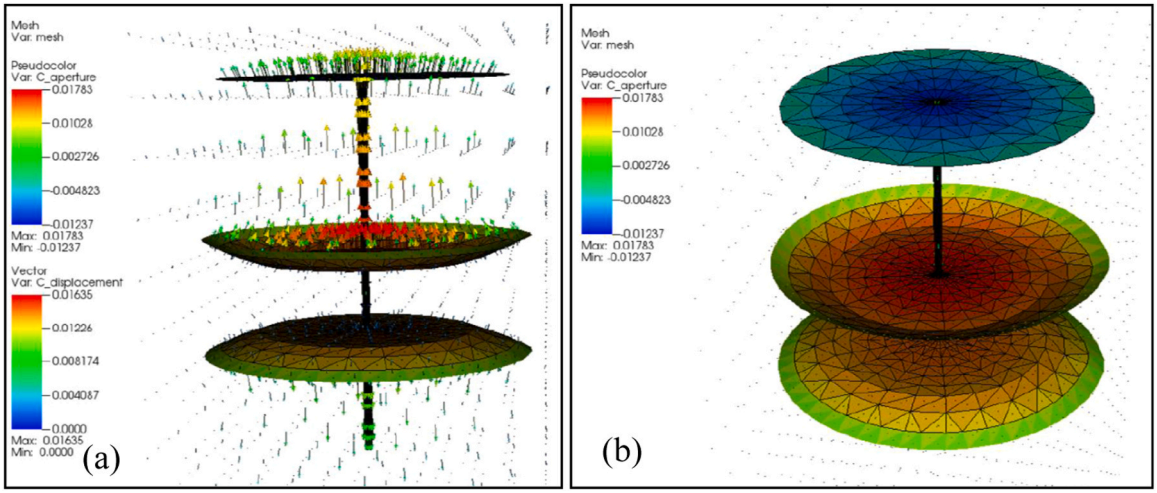

Fig. 15. FRACOD^{3D} simulation of two parallel horizontal fractures propagate due to fluid pressure in a vertical borehole. Configuration and aperture of fractures after 3 steps of propagation are shown. (a) displacement field and (b) aperture of fractures.

Table 2
Summary of modelling results of borehole breakout for Habanero #1 well.

σ_{Hmax} (MPa)	σ_{hmin} (MPa)	Breakout angle (°)	Normalised breakout depth (% of borehole radius)
80	60	117	28 %
80	40	90	31 %
80	25	81	37 %
80	10	72	32 %
70	50	86.4	24 %
70	30	72	24 %
70	15	72	26 %
60	50	64.8	16 %
60	40	57.6	14 %
60	30	57.6	26 %
60	20	64.8	20 %
60	11	57.6	29 %
50	30	14.4	5 %
50	20	36	20 %
50	10	43.2	24 %

correlation curve, likely attributable to constraints in numerical accuracy control and stochastic fracture initiation and propagation processes. To account for these variations, we incorporate both the mean values and the upper/lower bounds of the stress ratio-breakout depth relationship, as expressed in Eq. (37).

$$(3\sigma_{Hmax} - \sigma_{hmin}) \Big/ \sigma_c = 1 + A\left[\frac{r_d}{r}\right]^B \tag{37}$$

where

r_d = depth of breakouts measured from the original borehole wall

r = original radius of the borehole.

r_d/r = "normalised breakout depth".

A, B = the regression parameters to define the three curves in Fig. 17. Their values are: $A = 15.2$, $B = 2.67$ (average); $A = 21.2$, $B = 3.33$ (upper limit); $A = 12.6$, $B = 2.22$ (lower limit), respectively.

6.2.3. Back-analysis of the magnitude of principal horizontal stresses

When the breakout angle and its depth are known, the magnitudes of the major and minor horizontal principal stresses can be calculated by solving the system of equations defined by Eq. (36) and Eq. (37). The resultant expressions are as follows:

$$\sigma_{Hmax} = \frac{1 + (1 - 2\cos(\theta))\left(1 + A\left[\frac{r_d}{r}\right]^B\right)}{4(1 - \cos(\theta))} \quad \sigma_c \tag{38}$$

$$\sigma_{hmin} = 3\sigma_{Hmax} - \left(1 + A\left[\frac{r_d}{r}\right]^B\right)\sigma_c \tag{39}$$

These equations were then applied to estimate horizontal stress magnitudes within the Habanero #1 granite, utilizing the measured breakout geometry. Three distinct stress states were determined for each borehole depth: the average stress state, the upper-bound and the lower-bound stress states. The upper-bound and lower-bound values account for uncertainty in the estimated stress magnitudes.

6.3. Stress state in the Habanero #1 granite

Geophysical logging techniques have been employed to investigate borehole breakouts observed in the Habanero #1 granite formation. These logging data were analyzed to determine the angular extent and depth of breakouts at multiple positions along the wellbore within the granitic interval. The selected locations are those considered to have a representative borehole breakout angle and depth for a considerable length of the wellbore. They are also intended to cover the whole length of the granite section in the wellbore.

In order to provide statistical trends of stress distribution along the entire length of granite cross-sections, it is necessary to study an appropriate number of cross-sections at different depths. In this study, a total of 13 cross-sections were selected for retrospective analysis of stress states. Fig. 19 shows a typical image of the geophysical survey of the wellbore. For each cross-section, the breakout angle was measured from the images, whereas the extent of the breakout was obtained from the caliper logging results. Table 3 lists the measured breakout dimensions of all the 13 cross sections.

After determining the breakthrough angle and dimension, the magnitude of the horizontal stress is derived using Eqs. (38) and (39). Note that the calculated stress is effective stress. When calculating total stress, the pore pressure in granite is added which is equivalent to the mud pressure. Mud with a density of 1800 kg/m^3 was used during drilling, corresponding to a mud pressure of 74.1 MPa at a depth of 4209 m.

For each analysis scenario, the central tendency (mean) is used along with the upper and lower bounds to quantify parametric uncertainty. The predicted horizontal stress is shown in Fig. 20, and the stress ratio and predicted stress variation with depth are as follows. Note that all stresses obtained from subsequent analyses are total stresses, defined as effective stress plus pore pressure (equivalent to mud pressure).

Vertical stress was calculated using a granite density of 2670 kg/m^3 and sediment values derived from Hill et al. [55] for this region. The

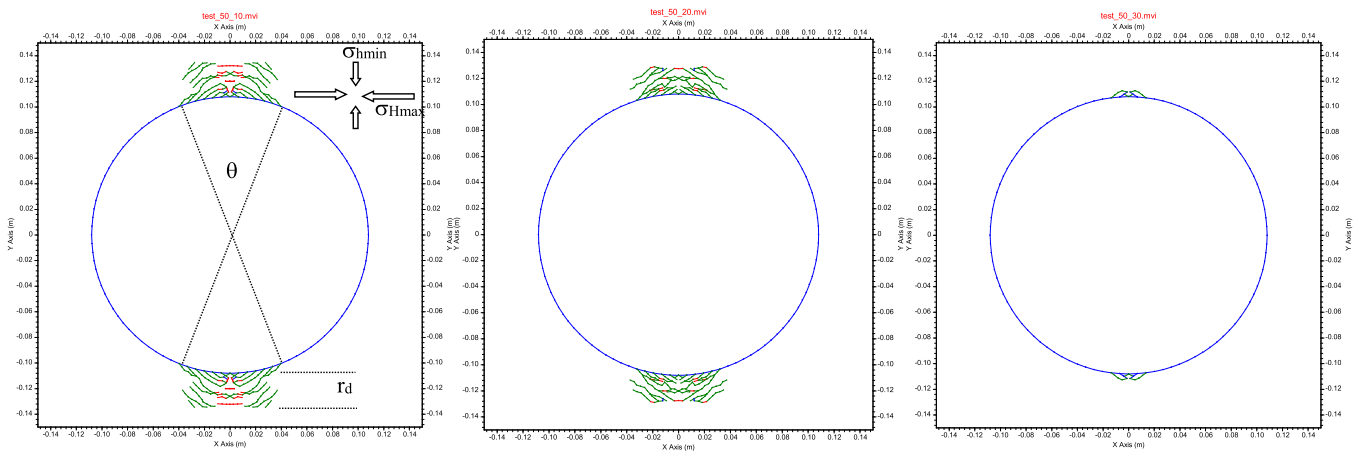

(a) σ_{Hmax}=50MPa, σ_{hmin}=10MPa **(b) σ_{Hmax}=50MPa, σ_{hmin}=20MPa** **(c) σ_{Hmax}=50MPa, σ_{hmin}=30MPa**

Fig. 16. Predicted borehole breakouts at σ_{Hmax} = 50 MPa and different σ_{hmin}. The definition of the breakout angle (θ) and depth (r_d) is also shown.

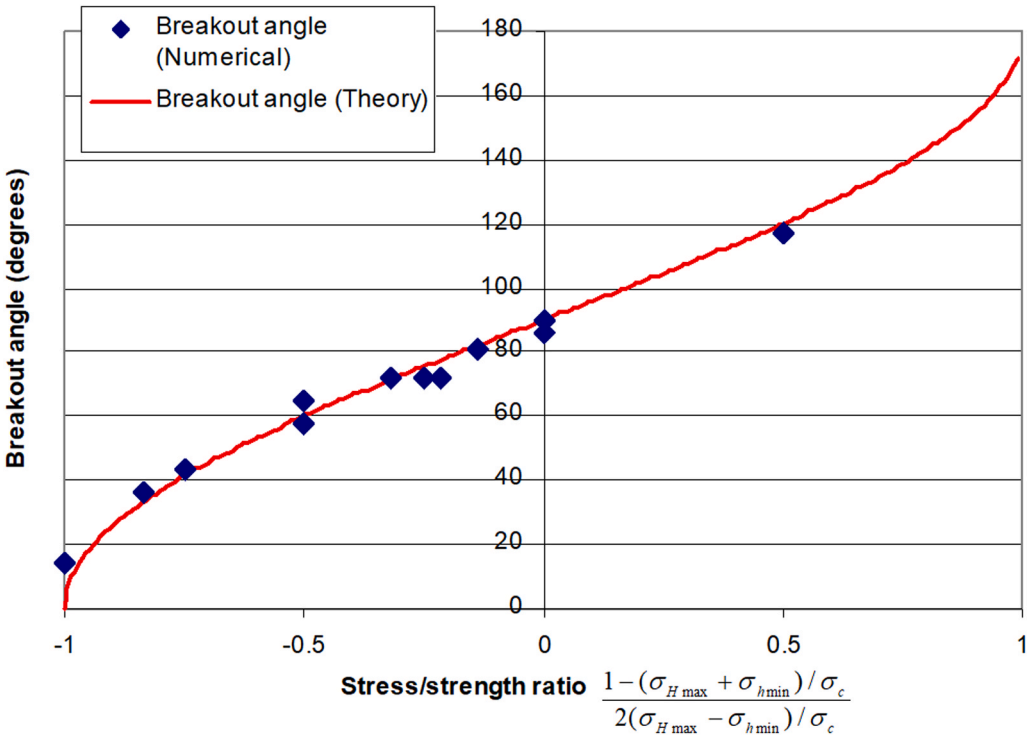

Fig. 17. Predicted relationship between stress/strength ratio and the breakout angle.

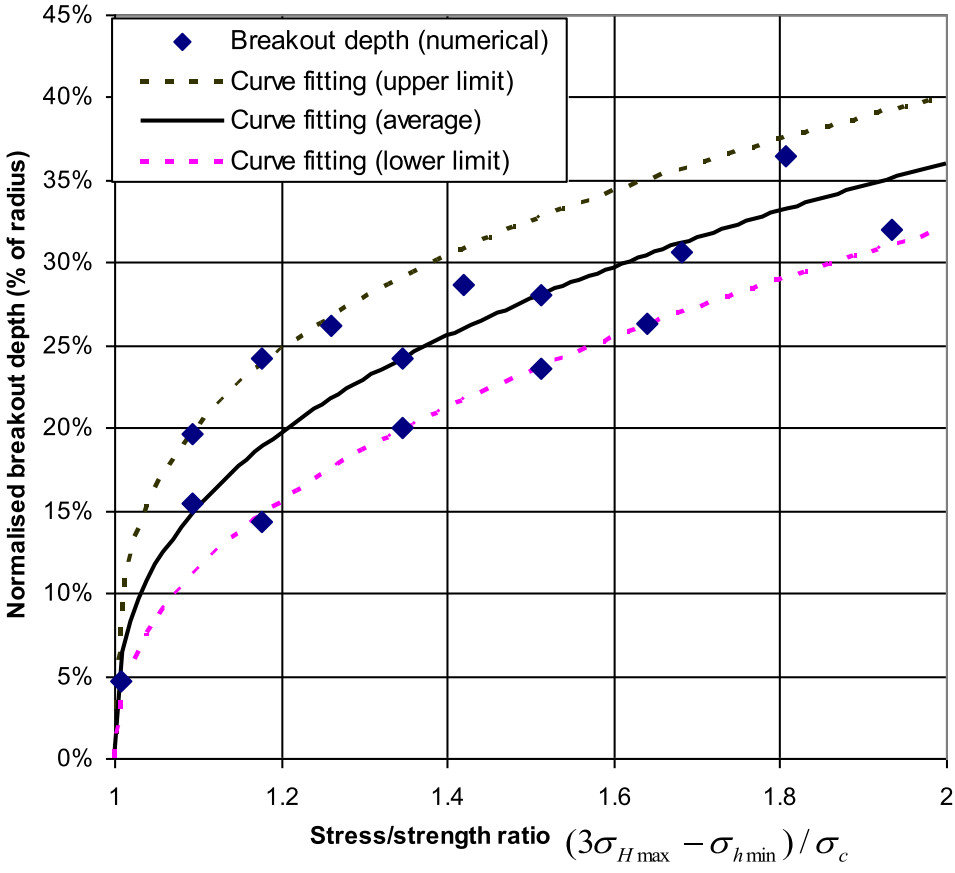

Fig. 18. Predicted relationship between stress/strength ratio and the normalised breakout depths.

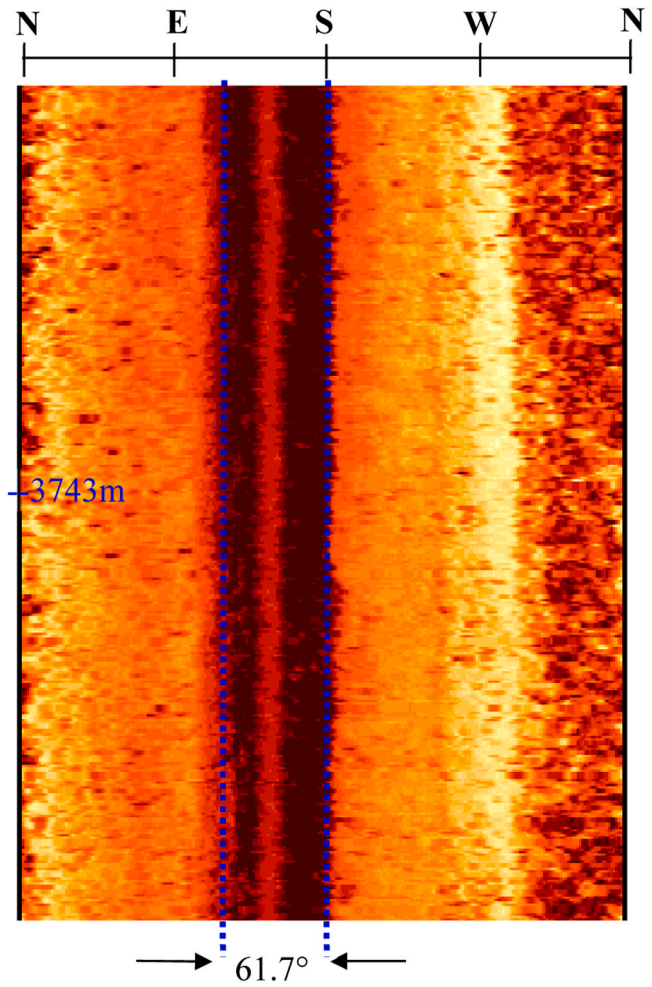

Fig. 19. Image of the geophysical survey of the wellbore at depth of 3743 m. The breakout angle was measured from the images, whereas the depth of the breakout was obtained from the caliper logging results (not shown in this figure).

Table 3
Measured borehole breakout dimensions at different depths.

Depth (m)	Breakout angle (°)	Normalised breakout depth (r_d/r)	Note
3728	67	6 %	
3743	61.7	8 %	Fig. 19
3776	72	13 %	
3810	61	9 %	
3885	66.8	14 %	
3923	61.7	18 %	
3968	61.7	24 %	
3996	66.9	17 %	
4033	61.7	18 %	
4109	61.7	18 %	
4121	72	22 %	
4142	72	15 %	

final results of the three principal stresses and their ratios to the vertical stress are given below.

Major horizontal principal stress: $\sigma_{H\max}$(total) = (0.033~0.034)·D (MPa)

Minor horizontal principal stress: $\sigma_{h\min}$(total) = (0.028~0.032)·D(MPa)

Vertical stress: σ_v (total) = 0.023·D(MPa)

Stress ratio:$\sigma_{H\max}/\sigma_{h\min}/\sigma_v$ (total) = (1.43~1.48)/(1.22~1.39)/1.00.

where D is the depth in meters.

It is important to note that the study results indicate the major and minor horizontal principal stresses both surpass the vertical stress at Habanaro #1 well granite. This implies that during any hydraulic fracturing operations in this wellbore, rock fractures would most likely propagate in the sub-horizontal directions, creating a sub-horizontal geothermal reservoir. This is an ideal situation for geothermal energy extraction operations as the *in situ* rock temperature in the reservoir is constantly high throughout the reservoir.

6.4. Seismic clouds during reservoir stimulation

Hydraulic stimulations were conducted by Geodynamics Ltd during 14 October 2003 – 17 January 2004 by injecting high pressure water into fracture zones at depth of 4140 m and below in the granite section of the wellbore [52]. A total of more than 18,000 m^3 water was injected into the rock mass during this period. Seismic activities during the stimulations were monitored using a microseismic monitoring system, and the interpretated seismic events are shown in Fig. 21. The seismic cloud suggests that the stimulated reservoir extended horizontally or sub-horizontally, possibly along several dominant natural fractures.

The stimulation results agree well with the FRACOD study results that the major and minor horizontal principal stresses both exceed vertical stress, i.e. a thrust-faulting stress regime. Only with this type of stress condition, the hydraulic fracturing events propagate in a sub-horizontal direction.

The FRACOD study was conducted before the hydraulic stimulation operations at Habanaro #1 well. It provided a valuable estimate of the *in situ* stresses that gave confidence and guide for the expensive stimulation operations. This investigation confirms that, when appropriate models accurately representing actual breakout mechanisms are employed, FRACOD models combined with measured breakout dimensions can serve as a reliable means of inferring *in situ* stress magnitude.

7. Conclusions

Rock fractures advance through both tensile and shear mechanisms. Accurately simulating mode II fractures plays a vital role in forecasting failure processes within rock masses. The numerical tool FRACOD employs fracture mechanics principles to simulate rock mass failure by explicitly representing the fracturing process. This computational approach utilizes the energy-based F-criterion to predict intricate mixed-mode fracture development in fractured rock formations.

Recent advancements in FRACOD have introduced new capabilities for coupled fracturing-thermal-hydraulic (F-T-H) simulations. The F-T coupling has been implemented through an indirect approach using the fictitious heat source methodology. The F-H coupling was achieved using an explicit approach and it employs an iterative scheme for both fluid flow and fracture propagation. The new function is capable of simulating fluid flow in complex fracture networks, and fracture movement and propagation driven by fluid pressure. A simple mechanism of fluid leakage into intact rocks has also been implemented.

In FRACOD, thermal-hydraulic (T-H) coupling accounts solely for fracture flow, modelling heat transfer in the rock as pure conduction and in the fracture fluid as pure convection. This model combines implicit methods in thermal analysis with explicit methods in fracture flow analysis, using an iterative solution scheme with a limited time step. Research has shown that this method can effectively predict the heat flow coupling process and has acceptable accuracy.

This paper presents the functionality and performance of FRACOD, including its Fracturing-Thermal-Hydraulic (F-T-H) coupled modules, through multiple case studies: biaxial loading tests, borehole cooling fractures, borehole breakout, and fluid flow and heat extraction in fractured geothermal reservoirs.

The paper also presents a case study utilizing FRACOD for back-analysis of *in situ* stresses in a deep geothermal wellbore. The FRACOD

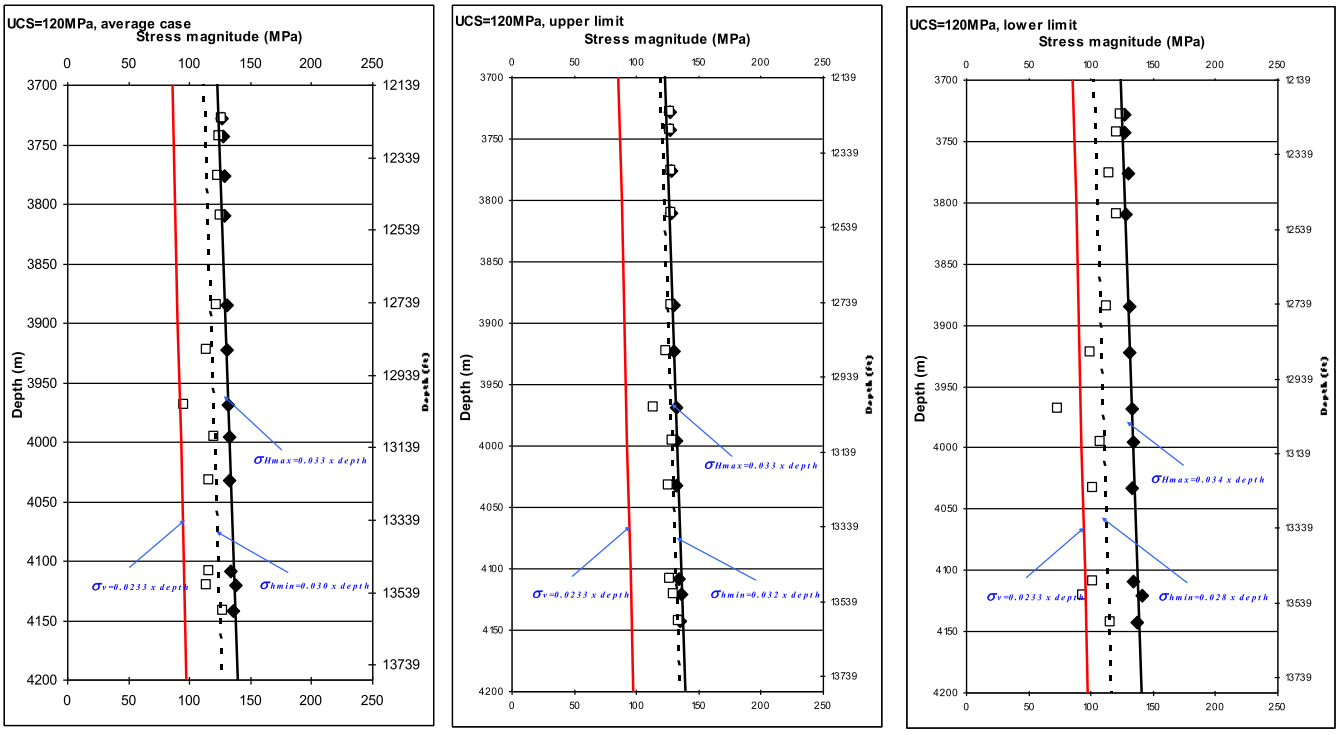

Fig. 20. Predicted *in situ* stress state in granite section of Habanero #1 well.

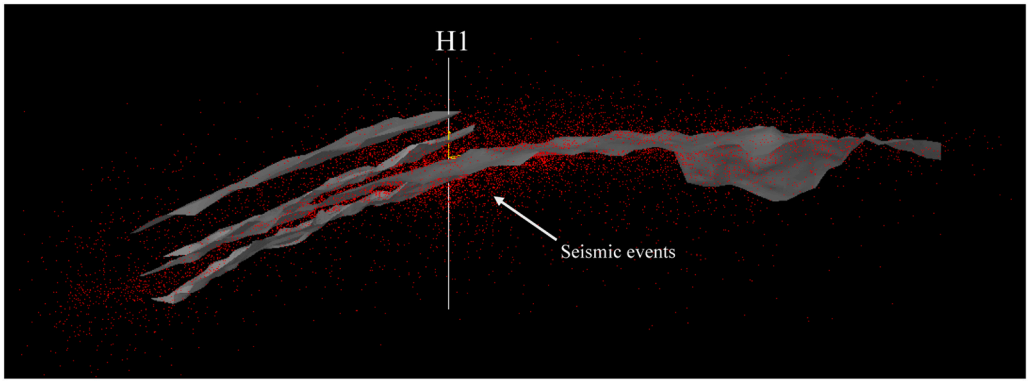

Fig. 21. Seismic clouds during reservoir stimulation.

study was conducted before the hydraulic stimulation operations and the stimulation results fully agreed with the results predicted by FRACOD model. This study demonstrates the feasibility of applying FRACOD to practical rock engineering problems when models accurately capture fundamental rock fracture mechanisms.

Recent developments in FRACOD have focused on extending the code to three dimensions, enabling true 3D fracture propagation and realistic simulation of underground excavation geometries. An example of FRACOD^{3D} application to three-dimensional fracture propagations driven by fluid pressure is also provided.

Compared with other commonly used numerical methods and codes for fracture propagation modelling, FRACOD has the advantage of representing rock fractures in an explicit way and directly employs rock fracture mechanics principles. This made it possible to handle complex fractures on an engineering scale. FRACOD, being a DDM based code, however has disadvantages in dealing with anisotropic and inhomogeneous problems. Future developments will focus on overcoming this shortcoming possibly by integrating other approaches with FRACOD.

CRediT authorship contribution statement

Baotang Shen: Writing – original draft, Visualization, Validation, Software, Resources, Project administration, Methodology, Investigation, Funding acquisition, Formal analysis, Data curation, Conceptualization.

Declaration of Competing Interest

The authors declare that they have no known competing financial interests or personal relationships that could have appeared to influence the work reported in this paper.

Acknowledgements

The author wishes to thank Prof Ove Stephansson and Prof Mikael Rinne who had been deeply involved in the FRACOD development from the very beginning. I would also like to thank our collaborative partners

in the International Collaboration Project on Coupled Fracture Mechanics Modelling, including but not limited to Prof. Yunliang Tan, Dr. Johannes Suikkanen, Dr. Eui Seob Park, Dr. Yongbok Jung, Dr. Kwang Yeom Kim, Dr. Li Zhuang, Prof. Xiaochun Li, Dr. Bin Bai, Prof. Chun'an Tang, Prof. Ki-Bok Min, Dr. Linmao Xie, Dr. Jonny Rutqvist, Prof. Simon Loew, Prof. Mikael Rinne, Prof Günter Zimmermann, Dr. Arno Zang, Dr Jeoung Seok Yoon, and Prof. Weiguo Liang. My appreciation is extended to my colleagues Dr Hua Guo and Dr Jingyu Shi for their involvement and support for many years. The help from Prof Bingrui Chen's team in modifying this paper to fit into the journal is gratefully appreciated.

References

[1] T.J. Boone, P.A. Wawrzynek, A.R. Ingraffea, Finite element modelling of fracture propagation in orthotropic materials, Eng. Frac. Mech. 26 (2) (1987) 185–201, https://doi.org/10.1016/0013-7944(87)90196-2.
[2] Y. Dong, B. Zeng, Y. Song, X. Zhou, P. Li, F. Zhang, Numerical study of hydraulic fracture propagation in orthotropic shale reservoirs by using the XFEM, Energy Fuels 37 (17) (2023) 12919–12933, https://doi.org/10.1021/acs.energyfuels.3c01627.
[3] J.S. Yoon, J. Hazzard, Chapter 10: coupled fracture modelling with distinct element methods, in: Shen, Stephansson, Rinne (Eds.), Modelling Rock Fracturing Processes - Theories, Methods, and Applications, 2014, Springer Nature Switzerland AG, 2020, pp. 227–254, https://doi.org/10.1007/978-3-030-35525-8.
[4] D. Tomporowski, M. Nitka, J. Tejchman, Application of the 3D DEM in the modelling of fractures in pre-flawed marble specimens during uniaxial compression, Eng. Frac. Mech. 277 (7) (2023) 108978, https://doi.org/10.1016/j.engfracmech.2022.108978.
[5] M. Cai, P.K. Kaiser, H. Morioka, M. Minami, T. Maejima, Y. Tasaka, H. Kurose, FLAC/PFC coupled numerical simulation of AE in large-scale underground excavations, Int. J. Rock. Mech. Min. Sci. 44 (4) (2007) 550–564.
[6] H. An, S. Wu, H. Liu, X. Wang, Hybrid finite-discrete element modelling of various rock fracture modes during three conventional bending tests, Sustainability 14 (2) (2022) 592, https://doi.org/10.3390/su14020592.
[7] X. Zhang, W. Xu, X. Zhang, Y. Yu, C. Xu, A hybrid finite-discrete element method for modelling cracking processes in sandy mudstone containing a single edge-flaw under cyclic dynamic loading, Sci. Rep. 14 (2024) 15346.
[8] K. Tazoe, H. Tanaka, M. Oka, G. Yagawa, An approach for fatigue crack propagation analysis by smoothed particle hydrodynamics method, Strength Fract. Complex. 12 (2-4) (2020) 127–133, https://doi.org/10.3233/SFC-190242.
[9] S. Yu, X. Ren, J. Zhang, H. Wang, Z. Sun, An improved form of smoothed particle hydrodynamics method for crack propagation simulation applied in rock mechanics, Int. J. Min. Sci. Techn 31 (3) (2021) 421–428, https://doi.org/10.1016/j.ijmst.2021.01.009.
[10] D. Mu, H. Qu, Y. Zeng, A. Tang, An improved SPH method for simulating crack propagation and coalescence in rocks with pre-existing cracks, Eng. Frac. Mech. 282 (2023) 109148, https://doi.org/10.1016/j.engfracmech.2023.109148.
[11] C. Xia, Z. Shi, H. Kou, A modified smoothed particle hydrodynamics method considering residual stress for simulating failure and its application in layered rock mass, J. Mt. Sci. 21 (2024) 2091–2112, https://doi.org/10.1007/s11629-023-8362-5.
[12] F. Sun, D. Liu, G. Wang, C. Cao, S. He, X. Jiang, S. Gong, Material point method simulation approach to hydraulic fracturing in porous medium, Eng. Anal. Bound. Elem. 162 (2024) 420–438.
[13] O. Reyes, H.H. Einstein, Failure mechanism of fractured rock – a fracture coalescence model, Proc. 7th Int. Con. Rock. Mech. 1 (1991) 333–340.
[14] B. Shen, O. Stephansson, H.H. Einstein, B. Ghahreman, Coalescence of fractures under shear stresses in experiments, J. Geophy. Res. 100 (B4) (1995) 5975–5990.
[15] B. Shen, Mechanics of fractures and intervening bridges in hard rocks. Doctorate Thesis (1993), Royal Institute of Technology, ISBN 91-7170-140-0.
[16] B. Shen, O. Stephansson, Modification of the G-criterion of crack propagation in compression, Eng. Frac. Mech. 47 (2) (1994) 177–189.
[17] B. Shen, O. Stephansson, Numerical analysis of mixed mode I and mode II fracture propagation. Special issue for the 34th U.S. Symposium of rock mechanics, Int. J. Rock. Mech. Min. Sci. 30 (1993) 861–867.
[18] M. Rinne. Propagation of rock fractures in the vicinity of a canister hole for spent nuclear fuel. Licentiate Thesis. Royal Institute of Technology, Engineering Geology. Stockholm, Sweden. ISBN 91-7170-617-8 (2000).
[19] B. Shen, O. Stephansson, M. Rinne, H.-S. Lee, L. Jing, K. Roshoff, A fracture propagation code and its applications to nuclear waste disposal, Int. J. Rock. Mech. Min. Sci. 41 (3) (2004) 448–449.
[20] M. Rinne, Fracture mechanics and subcritical crack growth approach to model time-dependent failure in brittle rock. Doctoral dissertation. Helsinki University of Technology, Rock Engineering. ISBN 978-951-22-9434-3. (2008). ⟨http://lib.tkk.fi/Diss/2008/isbn9789512294350/⟩.
[21] N. Barton, Rock Quality, Seismic Velocity, Attenuation and Anisotropy. Taylor & Francis Group, London, ISBN 0-415-39441-4. (2007).
[22] B. Shen, Borehole breakout and in situ stresses, SHIRMS 1 (2008) (2008) 407–418.
[23] B. Shen, H.M. Kim, E.S. Park, et al. Coupled Thermal-Fracture Behaviour of Rock: Laboratory Tests and Numerical Code Development. CSIRO Exploration and Mining Report P2008/2677 (2008).
[24] B. Shen, H.M. Kim, E.S. Park, T.K. Kim, M. Wuttke, M. Rinne, T. Backers, T. Meier, O. Stephansson, Multi-region boundary element analysis for coupled thermal-fracturing processes in geomaterials, Rock. Mech. Rock. Eng. 46 (2012) 135–151.
[25] L.M. Xie, K.B. Min, B. Shen, Displacement Discontinuity Method Modelling of Hydraulic Fracturing with Pre-Existing Fractures. Proceeding of 48th US Rock Mechanics/Geomechanics Symposium, ARMA 14-7464 (2014).
[26] T. Siren, I. Uotinen, M. Rinne, B. Shen, Fracture mechanics modelling of an in situ concrete spalling experiment, Rock. Mech. Rock. Eng. 48 (4) (2014) 1423–1438, https://doi.org/10.1007/s00603-014-0646-1.
[27] J. Shi, B. Shen, Approximation schemes of stresses on elements for the three-dimensional displacement discontinuity method, Eng. Anal. Bound. Elem. 48 (2014) 63–72.
[28] B. Shen, O. Stephansson, M. Rinne M. Modelling Rock Fracturing Processes: A Fracture Mechanics Approach Using FRACOD, 1st Edition, Springer, 2014 (publisher), 173p, ISBN 978-94-007-6903.
[29] B. Shen, O. Stephansson, M. Rinne. Modelling Rock Fracturing Processes: Theories, Methods, and Applications, 2nd Edition, Springer, 2020 (publisher), 573p, ISBN 978-3-030-35524-1.
[30] J.P. Petit, M. Barquins, Can natural faults propagate under mode II conditions? Tectonics 7 (6) (1988) 1243–1256.
[31] Q. Rao, Pure shear fracture of brittle rock – A theoretical and laboratory study. PhD Thesis, Lulea University of Technology (1999).
[32] T. Backers, O. Stephansson, E. Rybacki, Rock fracture toughness testing in mode II-punch-through shear test, Int. J. Rock. Mech. Min. Sci. 39 (6) (2002) 755–769.
[33] V.C. Li, Mechanics of shear rupture applied to earthquake zones, in: K.B. Atkinson (Ed.), Fracture Mechanics of Rock, Academic Press, London, 1991, pp. 351–428.
[34] S.L. Crouch, A.M. Starfield, Boundary element methods in solid mechanics, George Allen & Unwin, 1983.
[35] K.B. Min, J. Rutqvist, C.F. Tsang, L. Jing, Thermally induced mechanical and permeability changes around a nuclear waste repository—a far-field study based on equivalent properties determined by a discrete approach, Int. J. Rock. Mech. Min. Sci. 42 (2005) 765–780.
[36] J. Rutqvist, M. Chijimatsu, L. Jing, J. De Jonge, M. Kohlmeier, A. Millard, T. S. Nguyen, A. Rajeb, M. Souley, Y. Sugita, C.F. Tsang, Numerical study of the THM effects on the near-field safety of a hypothetical nuclear waste repository – BMT1 of the DECOVALEX III project. Part 3: effects of THM coupling in fractured rock, Int. J. Rock. Mech. Min. Sci. 42 (2005) 745–755.
[37] C.F. Tsang, L. Jing, O. Stephansson, F. Kautsky, The DECOVALEX III project: a summary of activities and lessons learned, Int. J. Rock. Mech. Min. Sci. 42 (56) (2005) 593–612.
[38] B. Shen, H. Guo, T.Y. Ko, S.C. Lee, J. Kim, H.M. Kim, E.S. Park, M. Wuttke, T. Backers, M. Rinne, O. Stephansson. coupling rock fracture propagation with thermal and fluid flow processes, Int. J. Geomech. 13 (2013) 794–808.
[39] Itasca, UDEC Version 7.0 – Distinct Element Modelling of Jointed and Blocky Material in 2D. Itasca Consulting Group, Inc., Minneapolis, MN 55401, USA (2024).
[40] C. Louise, A Study of Groundwater Flow in Jointed Rock and Its Influence on the Stability of Rock Masses. Imperial College, Rock Mech. Research Report No.10 (1969).
[41] B. Shen, O. Stephansson, M. Rinne, Simulation of borehole breakouts using FRACOD2D, Oil & Gas Science and Technology - Revue de l'IFP, special issue for International Workshop of Geomechanics in Reservoir Simulation – 5 to 7 December 2001 – IFP. Rueil-Malmaison, France 57 (5) (2002) 579–590.
[42] G. Klee, A. Bunger, G. Meyer, F. Rummel, B. Shen, In situ stresses in borehole blanche-1/South Australia derived from breakouts, core discing and hydraulic fracturing to 2 km depth, Rock. Mech. Rock. Eng. 44 (2011) 531–540.
[43] N. Barton, B. Shen, Risk of shear failure and extensional failure around over-stressed excavations in brittle rock, J. Rock. Mech. Geotech. Eng. 9 (2) (2017) 210–225.
[44] M. Rinne, B. Shen, H.S. Lee, L. Jing, Thermo-mechanical simulations of pillar spalling in SKB APSE test by FRACOD. GeoProc International Symposium, Stockholm, Sweden, August (2003).
[45] O. Stephansson, B. Shen, M. Rinne, et al., Geomechanical evaluation and analysis of research shafts and galleries in MIU Projects, Japan. In: Environmental Rock Engineering. Proceedings the 1st Kyoto International Symposium on Underground Environment – Role of Geo-technology to the Underground Environment. March 17-18 Kyoto Japan (2003), 39-45.
[46] B. Shen, O. Stephansson, M. Rinne, K. Amemiya, R. Yamashi, S. Toguri, H. Asano, FRACOD modelling of rock fracturing and permeability change in excavation-damaged zone, Int. J. Geomech. 11 (2011) 302–331.
[47] M. Rinne, B. Shen, Numerical simulation of core tests using FRACOD in Understanding and characterizing of the Excavation Disturbed Zone (EDZ).

DECOVALEX Task B Phase 2 report. In Hudson and Jing 2007. SKI Report 2007:08. Swedish Nuclear Power Inspectorate. (2007).
[48] B. Shen, J. Shi, Analysis of Fracturing-Hydraulic coupling in transversely isotropic rocks and a case study on CO2 sequestration, Int. J. Rock. Mech. Min. Sci. 88 (2016) 206–220.
[49] G. Bodvarsson, On the temperature of water flowing through fractures, J. Geophy. Res. 74 (8) (1969) 1987–1991.
[50] J. Shi, B. Shen, O. Stephansson, M. Rinne, A three-dimensional crack growth simulator with displacement discontinuity method, Eng. Anal. Bound. Elem. 48 (2014) 73–86.
[51] J. Shi, B. Shen, FRACOD3D: a Three-Dimensional crack growth simulator code, in: Shen, Stephansson, Rinne (Eds.), Modelling Rock Fracturing Processes - Theories, Methods, and Applications, 2014, Springer Nature Switzerland AG, 2020, pp. 135–172, https://doi.org/10.1007/978-3-030-35525-8.
[52] Geodynamics Ltd, Habanero #1 Stimulation Operation Review. Geodynamics Ltd report (2004).
[53] B. Shen, X. Tan, C. Li, O. Stephansson, Simulation of borehole breakout using fracture mechanics models, in: Sugawara, Obara (Eds.), In: Rock Stress, Balkema, Rotterdam, 1997, pp. 289–298.
[54] B. Shen, O. Stephansson, M. Rinne, Simulation of borehole breakouts using FRACOD2D, Oil Gas. Sci. Technol. Rev. IFP 57 (5) (2002) 579–590.
[55] R.R. Hill, J.J. Meyer, M.E. Magee, The contemporary Stress Field of the Nappamerri Trough and Its Implications for Tight Gas Resources. Report of Department of Geology and Geophysics, University of Adelaide, SA 5005, Australia (1997).

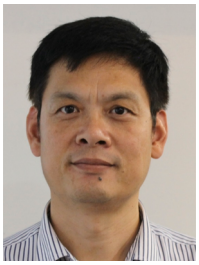

Dr. Baotang Shen was a Senior Principal Research Scientist at CSIRO Mineral Resources, and currently a Professor at Shandong University of Science and Technology. He graduated from the Department of Mining Engineering, Northeastern University in 1985; Obtained PhD from Royal Institute of Technology (KTH), Sweden in 1993; Visiting Scholar at Massachusetts Institute of Technology (MIT) in 1993; Postdoc Research Fellow at Norwegian Geotechnical Institute (NGI) in 1994. Since 1995, he has been working with the CSIRO, Australia. Dr. Shen's main research areas are: Rock mechanics, Rock fracture mechanics; Deep mining engineering, Mining environmental engineering. He has been leading CSIRO's research team on mine subsidence control and mine remediation, and developed the non-cohesive backfill technology for old mine remediation. The team has completed several major projects funded by Australian Coal Association Research Program (ACARP) and BHP Billiton Illawarra Coal and Queensland State Government on subsidence control and remediation technologies for a number of mines in Australia. Dr Shen is an influential expert in fracture mechanics modelling. He has initiated and led an international collaboration project on coupled fracture mechanics modelling, which is participated by 13 institutes from Germany, Finland, Switzerland, South Korea, China, USA and Australia. He is also the leading author of two published books: "Modelling Rock Fracturing Processes – A fracture mechanics approach using FRACOD"; "Modelling Rock Fracturing Processes – Theories, Methods, and Applications". He has published more than 190 research papers in international journals and conference proceedings which has total citations of more than 5000 times.